2014

Nondestructive Analysis of Advanced Aerospace Materials via Spectroscopy and Synchrotron Radiation

Albert Manero
University of Central Florida

NONDESTRUCTIVE ANALYSIS OF ADVANCED AEROSPACE MATERIALS VIA SPECTROSCOPY AND SYNCHROTRON RADIATION

by

Albert C. Manero II
B.S. University of Central Florida, 2012

A thesis submitted in partial fulfillment of the requirements
for the degree of Master of Science
in the Department of Mechanical and Aerospace Engineering
in the College of Engineering and Computer Science
at the University of Central Florida
Orlando, Florida

Spring Term
2014

Major Professor:
Seetha Raghavan

Abstract

Advanced aerospace materials require extensive testing and characterization to anticipate and ensure their integrity under hostile environments. Characterization methods utilizing synchrotron X-Ray diffraction and spectroscopy can decrease the time required to determine an emerging material's readiness for application through intrinsic information on the material response and failure mechanisms. In this study, thermal barrier coating samples applicable to turbine blades of jet engines were studied using Raman and Photoluminescence spectroscopy as well as Synchrotron X-ray diffraction while Kevlar®-based fiber composites applicable to ballistic resistant armor were studied using Raman spectroscopy to investigate the mechanical state and corresponding damage and failure mechanisms.

Piezospectroscopic studies on the stress state of the thermally grown oxide (TGO) within the thermal barrier coatings, on a hollow cylindrical specimen, provided results that indicate variations within the TGO. Comparison of measured photo-luminescence spectra of the specimen before and after long duration thermal aging showcases the development of the system and the initiation of micro-damage. Raman spectroscopy performed on Kevlar® ballistic composites with nanoscale additives, presented insight into the additives' role in load transfer and damage propagation through a comparison of the shift in optical spectra to that of the pristine fibers.

The results presented herein utilize changes in the measured emission from these non-destructive testing techniques to link the phenomena with material response. Techniques to optimize imaging and spectral collection are addressed as well. The findings will advance the use of the techniques in the development of aerospace materials, providing a more complete understanding of land and aircraft turbine blade coatings, and fiber composite response to complex loading.

"Every formula which expresses a law of nature is a hymn of praise to God."

- Maria Mitchell

Acknowledgments

My exceeding thanks to my family for supporting me through this journey and to my lovely Katie for standing beside me. To my research advisor and Thesis Chair, Dr. Seetha Raghavan, for support and guidance on the project. To my committee members Dr. Jihua Gou and Dr. Jeffrey Kauffman for their participation, and continued support. To my colleagues at the University of Central Florida who assisted in the project: Kevin Knipe, Gregory Freihofer, Jason Gibson, and Stephen Sofronsky. To Dr. Marion Bartsch for her support of the project. This material is based upon work supported by the National Science Foundation grants (Grant Nos. OISE 1157619, CMMI 1130837, and CMMI 1125696) and by the German Science Foundation (DFG) grant (Grant No. SFB-TRR103), Project A3. Use of the Advanced Photon Source, an Office of Science User Facility operated for the U.S. Department of Energy (DOE) Office of Science by Argonne National Laboratory, was supported by the U.S. DOE under Contract No. DE-AC02-06CH11357.

TABLE OF CONTENTS

LIST OF FIGURES xi

LIST OF TABLES xvii

CHAPTER 1 INTRODUCTION 1

1.1 Motivation and Background 1

1.1.1 Applications of Piezospectroscopy and Synchrotron Radiation for Material Characterization 2

1.2 Overview of Research 7

CHAPTER 2 PIEZOSPECTROSCOPY AND DIFFRACTION METHODS . . 9

2.1 Piezospectroscopy 9

2.1.1 Photoluminescence Spectroscopy 9

2.1.2 Raman Spectroscopy 11

2.1.3 Collection Methods 12

2.1.4 Fitting Methods and Analysis 13

2.2 Synchrotron Radiation 13

2.2.1 X-Ray Diffraction Techniques 14

2.2.2 Collection Methods 16

2.2.3 Fitting Methods and Analysis Procedures 17

CHAPTER 3 SPECIMEN MATERIALS, GEOMETRY, AND EXPERIMENTAL SETUP 19

3.1 Thermal Barrier Coating System 19

3.1.1 Sample Design 19

3.1.2 Material Properties 22

3.1.3 Experimental Design, Loading Conditions, and Measurement Methods for the Study of Thermal Barrier Coatings 23

3.2 Kevlar® Ballistic Panels 37

3.2.1 Sample Design 37

3.2.2 Material Properties 39

3.2.3 Experimental Design, Loading Conditions, and Measurement Methods for Kevlar® Composites 44

CHAPTER 4 PIEZOSPECTROSCOPIC STUDY OF THERMAL BARRIER COATING SYSTEMS 48

4.1 Objectives 48

4.2 Photoluminescence of Thermally Grown Oxide From Early Cyclic Aging 49

4.3 Raman Spectroscopy of Yttria-Stabilized Zirconia Top Coat From Early Cyclic Aging 58

4.4 Comparison of Early Cycling vs. Aged Specimen 65

4.4.1 Photoluminescence of Thermally Grown Oxide Following Long Duration Aging 65

4.4.2 Raman Spectroscopy of Yttria-Stabilized Zirconia Top Coat Following Long Duration Aging 70

4.5 Conclusions 74

CHAPTER 5 X-RAY DIFFRACTION FOR STRAIN ANALYSIS OF THERMAL BARRIER COATING SYSTEMS 76

5.1 Objectives 76

5.2 Discussion of Results 77

5.2.1 Phase Identification 79

5.2.2 Strain Profiles of MCrAlY Bond Coat 83

5.2.3 Strain Profiles of Yttria-Stabilized Zirconia Top Coat 84

5.3 Conclusions 85

CHAPTER 6 PIEZOSPECTROSCOPIC STUDY OF KEVLAR® BALLISTIC PANELS 87

6.1 Objectives 87

6.2 Discussion of Results 88

6.3 Additive Effects of Load Transfer 90

6.4 Conclusions 94

CHAPTER 7 CONCLUSIONS AND FUTURE OUTLOOK 96

LIST OF REFERENCES 101

LIST OF FIGURES

1.1 Schematic of the Loading Conditions Applied to a Turbine Blade in Application 4

2.1 Photoluminescence Spectroscopy Theory Relating Excitation to Resulting Characteristic Optical Spectra 10

2.2 Raman Spectroscopy Theory Relating Excitation to Resulting Characteristic Optical Spectra 12

2.3 Fundamentals of X-Ray Diffraction: A) Schematic of Synchrotron Light Source B) Bragg's Law Relating Crystalline Planes to Diffraction Angle C) Debye-Scherrer Rings Collected by a 2D Area Detector D) Strain Curve Fit for a Single Measurement 15

2.4 Method 1: Grazing surface from 5 to 100 μm. 2D detector measures axial and radial components of strain. By moving the sample into the beam, each layer can be scanned and collected. Method 2: Direct transmission along center line. 2D detector measures wall-thickness averaged axial and circumferential components of strain. [114] 17

2.5 Strain Fitting Procedure: A) Transformed Lineout Plot Around Azimuth B) Discretized Transform Bin for Fitting C) Fit Strain Curve 18

3.1 Thermal Barrier Coating System 20

3.2 As Coated Sample CAD 21

3.3 As Coated TBC Specimen 22

3.4 Design and Description of Loading Conditions for in-situ X-Ray Diffraction Study 25

3.5 Design of Thermal Gradient and Mechanical Loading for X-Ray Diffraction Measurements 26

3.6 Representative Thermal Cycle 27

3.7 Scanning Window for X-Ray Diffraction 28

3.8 Specimen in Thermal Gradient and Mechanical Loading Apparatus . . . 30

3.9 Estimated TGO Thickness after 17 Cycles 31

3.10 Piezospectroscopic Scanning Zones 32

3.11 Portable Spectrometer for Piezospectroscopic Measurements. 33

3.12 Piezospectroscopic Scanning Zones for Aged Specimen 36

3.13 Molecular Structure of Kevlar® (Left), its Orientation in a Kevlar® Fiber (Center), and Pristine Weave (Right) 38

3.14 Scanning Electron Microscopy of Baseline Kevlar® Composite [51]. *Image Credit*: *Jason Gibson* 40

3.15 Baseline Kevlar® 29 Panel Composite 41

3.16 Scanning Electron Microscopy of CNT Additive to Kevlar® Composite [51]. *Image Credit*: *Jason Gibson* 42

3.17 Tunneling Electron Microscopy of CSR Kevlar® Composite [51]. *Image Credit*: *Jason Gibson* 43

3.18 A) Carbon Nanotube Additive Panel and B) Core Polymer Ball Additive Panel 44

3.19 Mapping Routine for Ballistic Damage for Kevlar® Panels 46

3.20 Limitations in Scanning 47

4.1 Scanning Schematic for Conducting Photoluminescence on Thermally Grown Oxide and the Optical Spectra Collected 49

4.2 Collected Optical Spectra on CCD 50

4.3 A) Optical Spectra of Thermally Grown Oxide with Phase Identification B) Fitted Doublet Peak for α-Phase Alumina 50

4.4 Biaxial Assumption for Thin Films and Thermal Expansion Mismatch [59] 52

4.5 Stress Map of the Thermally Grown Oxide on an Early Aged Specimen by Photoluminescence via R1 Optical Peak 53

4.6 Linking Thermal Variations with TGO Stress 55

4.7 Stress Map of the Thermally Grown Oxide on an Early Aged Specimen by Photoluminescence via R2 Optical Peak 56

4.8 Map of the Thermally Grown Oxide Stress Deviation Percentage as Calculated via the R1 and R2 Optical Peaks 57

4.9 Collected Optical Spectra of Yttria-Stabilized Zirconia on CCD 58

4.10 The Raman Spectra of Yttria-Stabilized Zirconia 59

4.11 Peak Fitting for Yttria-Stabilized Zirconia 60

4.12 Collected Optical Spectra of Yttria-Stabilized Zirconia via Micro-Raman for Identification of Peak Close to Laser Line 61

4.13 Raman Peak Shift Map from Zero Reference of 258 cm^{-1} 62

4.14 Raman Peak Shift Map from Zero Reference of 638 cm^{-1} 64

4.15 TGO Stress Map (R1) of an Aged Specimen with Identified Microdamage 66

4.16 Dual Stress States Presented in Scan Over Micodamaged Zone with 3GPa Variation 67

4.17 Observed Micro Damage 68

4.18 Stress Map of Aged Oxide via R2 Optical Peak 69

4.19 Difference of the Resulting Stress Values from R1 and R2 Peaks of α-Alumina via Photoluminescence 70

4.20 Peak Location Map for Aged Zirconia (Peak 258 cm^{-1}) 71

4.21 Peak Location Map for Aged Zirconia (Peak at 638 cm^{-1}) 71

4.22 Map of the Shift in Peak Center from Early Cycled to Long Duration (Peak at 258 cm^{-1}) 72

4.23 Map of the Shift in Peak Center from Early Cycled to Long Duration (Peak at 638 cm^{-1}) 73

5.1 X-Ray Diffraction Scanning Location and Applied Loading Conditions . . 77

5.2 Representative Flight Cycle for in-situ Measurements 78

5.3 Scanning Locations Across the Coating System 79

5.4 Phase Identification Conducted for a TBC Specimen [71] 80

5.5 Strain Invariant Angle Determination for Strain Analysis 81

5.6 Intensity vs. D-Spacing Plot Through Thermal Cycle with Visible Undulations Due to Thermal Expansion in Response to Thermal Loading . . . 82

5.7 In-Situ Strain Profile for MCrAlY Bond Coat in Response to Representative Flight Cycle [70] 83

5.8 Strain Profile for YSZ in Response to a Representative Flight Cycle [70] . 85

6.1 Scanning Objectives of Ballistic Damage on Kevlar® Composite Panel . 87

6.2 Pristine Kevlar® Fiber's Optical Spectra and Identification of Molecular Structure 88

6.3 Linking the Molecular Structure and Piezospectroscopic Measurements to Load Transfer Throughout the Composite 91

6.4 Additive's Effect on Piezospectoscopy Compared with Ballistic Resistance Performance 93

7.1 Application of Customized Stress and Damage Sensitive Composite Coatings for Use in Non-Destructive Testing of Aerospace Vehicles. [54] *Image Credit*: *Dave Thomas* 99

LIST OF TABLES

3.1 High Temperature and Room Temperature Material Properties for Thermal Barrier Coating System on IN100 Substrate [60] 23

3.2 Material and Mechanical Properties of Kevlar® 29 and Kevlar® 49 [43] 39

3.3 Kevlar® 29 Raman Properties, Theoretical vs. Experimental Results [20, 69, 101, 134] 39

6.1 Tabulated Raman Readings for Pristine Fibers 89

6.2 Resulting Peak Centers for Pristine, Literature, Baseline, and Additive Panels with Statistical Data 92

CHAPTER 1
INTRODUCTION

1.1 Motivation and Background

Nondestructive testing methods have been a necessity for industrial applications for nearly a century. [107] At its inception, visual inspection was required in an effort to avoid mechanical failures due to fatigue and oxidation [107, 33]. In this time, novel techniques have been pioneered to provide access to many forms of intrinsic information from structures and materials. However, the true potential of many of these techniques has yet to be actualized. To probe materials and mechanical systems, a variety of methods have been employed including radiation, sound waves, vibrations, and magnetic waves. [13, 42, 143, 91] The common applications have included material identification, material and joint integrity, crystal grain growth, and visual qualitative identification of damage. [104, 19, 48] These complex techniques require further research to continue to unlock their vast potential to reveal details on the mechanics of material response. The study herein will explore piezospectroscopic and diffraction techniques which probe the molecular response of materials, in an effort to link the micro phenomena to the bulk response. This provides novel information for materials and composites which benefits the development of emerging aerospace materials while ensuring their integrity under the extreme conditions of operation.

A great deal of research has been conducted to look at materials and mechanical equipment outside their normal operation regimes due to the complexity of testing under operational conditions. Taking the material from its service conditions to the laboratory allows for inspection techniques, providing the capability to assess the effects of operational environments on structures and materials. The effects of loading are observed, while the mechanisms of damage or fatigue are generally deduced from these observations. Herein, the studies will showcase the ability to conduct measurements to consider the dynamic response of the structures and materials under loading conditions and the residual states following the loading conditions.

1.1.1 Applications of Piezospectroscopy and Synchrotron Radiation for Material Characterization

Aerospace applications require very high design tolerance, long lifetimes, and minimum weight to assure their functionality. As a consequence, elaborate and highly tailored composites have been designed for their unique role in the mechanism of vehicle's design. Multi-layer coatings, fiber composites, ceramic matrix composites, and metal matrix composites have all been uniquely designed for various applications. [64, 88, 97, 112]

For both aircraft thrust and land based power generating engines, aerodynamic turbine blades are employed to extract or impose energy in the flow. The increasing high temperature combustion gases required to drive these powerful engines have continued

to raise the efficiency of the system. [10] Recently, more work has been done to increase the inlet temperatures to gain additional efficiency. [29, 89, 82] This is due in part that a mere 1 percent increase in efficiency can save $200,000 in fuel cost per year for a gas powered turbine. [102]

Thermally Barrier Coatings began their development almost 50 years ago to mitigate the high temperature effects on the turbine blade superalloys. [77, 76, 18] Operational temperatures have since been exceeded in order to increase the overall performance of the engine. To do so, thermal barrier coatings have been employed to separate the underlying load bearing metal from the high temperature combustion gases. This imposes a thermal gradient over the multi-layer coating system, protecting the substrate. The thermal gradient has allowed for longer use of turbine blades, increased operating temperatures, and increased reliability. [98, 35, 25, 141, 8, 47, 7] A schematic representation of this is detailed in Figure 1.1. However, if the coating should fail, the extreme temperatures can quickly damage the turbine blade. In industry, these downtimes lead to costly financial penalties. Of key interest to the aerospace community is to determine the failure mechanisms responsible for the different types of failure, commonly seen in application. [61, 58, 106, 95, 75, 93, 15, 12, 16, 23, 24, 9] Utilizing these testing methods this study will investigate the effects of long duration aging on thermal barrier coatings to identify failure and damage mechanics, and apply the methods to additional aerospace composites.

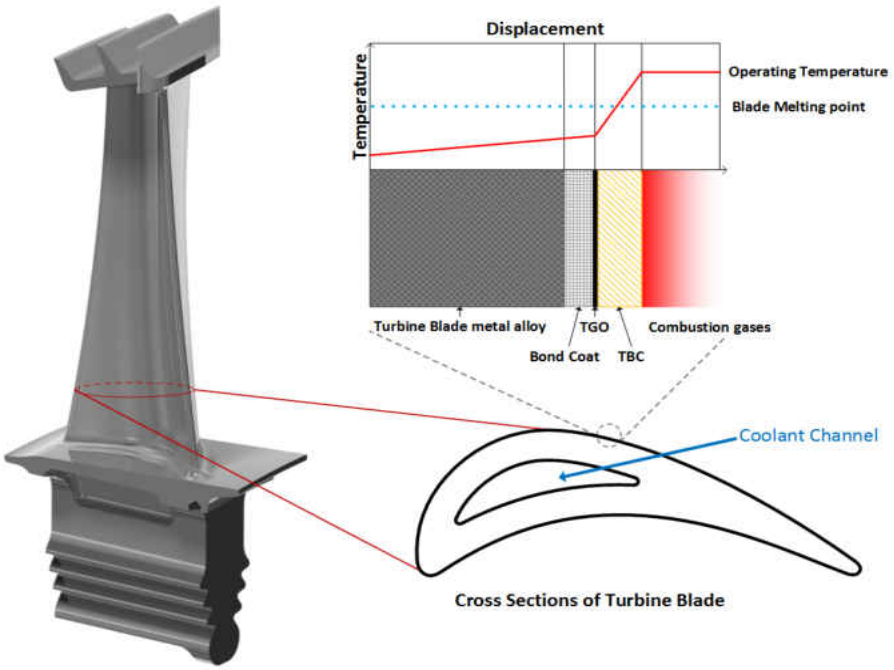

Figure 1.1: Schematic of the Loading Conditions Applied to a Turbine Blade in Application

The thermal barrier coating system is traditionally made of a ceramic top coat and a metallic bond coat adhered to the substrate superalloy. From the onset of the coating process, a thin thermally grown oxide of alumina develops between the bond coat and ceramic top coat. This layer, which grows with time under thermal loads, is effective for halting the transport of oxygen deeper into the multi-layer system. Investigation has been conducted into understanding the mechanics of growth in the thermally grown oxide and how that affects the overall performance and degradation of the system. [45, 57, 60, 67, 3, 47, 108] Damaged turbine blades are commonly observed to have coating damage

and spallation on areas of curvature. [31] This leaves the superalloy substrate vulnerable to the high temperature combustion gases, leading to ultimate failure of the blade.

Previous work has been conducted to identify how the thermally grown oxide behaves under cycling from its coating till its eventual failure. [60, 68, 46, 37, 96, 26] Christensen et al. and Nychka et al. showed ex-situ Photoluminescent spectroscopy studies of the oxide layer for damage quantification and determining the residual stress state. The measurements were conducted for isothermal loading conditions. It has been observed that the loading conditions during the aging process have an effect on the results found in the ex-situ study. [65, 100, 125] Additional studies have also shown variations due to the sample's geometry [115, 100] and the influence of induced cooling gradients [113, 40, 14, 142]. Capturing the effects of realistic geometries and applied loading conditions is critical to developing a complete understanding of thermal barrier coatings' performance and failure.

Raman Spectroscopy is another powerful tool that has been used to investigate vibrational energy in Raman active materials. Much work has been done to fingerprint material composition and identify residual stress from manufacturing. [74, 110, 119, 124, 32, 34, 90] This work has been effective in providing information during material synthesis, following high temperature, and for determining the residual stress state of some aerospace materials. [39, 110, 85, 83] This study investigates the use of Raman Spectroscopy to investigate the top most layer of the Thermal Barrier Coating System, the ceramic top coat. Classical Thermal Barrier Coatings have utilized Yttria-Stabilized Zirconia which

has a known characteristic optical spectra. One of the aims of this work is to apply these non-invasive techniques to identify system wide effects of thermally grown oxide's development by using spectroscopy on the ceramic top coat. The oxide may be scanned, as the columnar structure of the ceramic top coat produced by Electron-Beam Physical Vapor Deposition is semi-transparent to visible light. However for layers deeper in the coating system, different techniques are needed in order to penetrate the layers.

X-Ray diffraction is a technique that extends the capability of investigating the Thermal Barrier Coating system. Common lab equipment has produced interesting data on the material using backscattering methods including material identification for composites and changes of material phase following high temperature holds. [140, 66, 22] The lack of depth penetration and the limitations of 1D detectors have kept this technique from being fully realized for optimum testing. [55] Increases in energy and throughput, coupled with advances in detectors and optics, have led to even more effective research methods. X-Ray diffraction measures changes in the spacing of the crystal lattice planes, of which a measurement of strain can be collected from this Angstrom deviation of the crystalline lattice spacing. [37, 32, 62, 36]

This work will utilize synchrotron X-Ray diffraction to identify the in-situ strain profile of a complex geometry Thermal Barrier Coating and superalloy substrate with realistic imposed loading conditions to more completely understand the performance and failure mechanisms in cycle.

1.2 Overview of Research

An examination of non-destructive testing techniques for application in determining material readiness for commercial application, providing in-situ measurements for remote testing, and non-invasive examinations of sensitive equipment is of great interest to both industry and the research community. In environments deemed too harsh or simply inaccessible for human measurement, novel methods for identifying damage and predicting failure are to be explored. Analysis of material properties and loading response under working conditions can provide valuable information for advancing novel material's application into industry. Currently a lack of material properties and response for complex geometry and realistic loading conditions limits our understanding of failure mechanisms and lifetime expectancy for aerospace materials. Herein a discussion of the motivation behind the research is discussed, aimed at gas turbine blades and advanced fiber composites. An overview of non-destructive testing techniques will also be developed. In Chapter 2 an introduction to the theory and measurement methods is detailed, including Raman Spectroscopy, Photoluminescence Spectroscopy, and Synchrotron X-Ray Diffraction techniques. Data analysis and fitting procedures for developing strain and stress profiles and identifying damage is also outlined. The specimen materials, geometry, and experimental setup are detailed in Chapter 3. Specimen design and manufacturing is presented, and material properties and methodology of loading and measurements techniques are described. A combination of non-destructive testing techniques on the selected

materials is discussed. Results of the piezospectroscopic studies on thermal barrier coatings are presented in Chapter 4, including a comparison of findings from the early cycled specimen versus the aged specimen. In Chapter 5, a discussion of results of the X-Ray diffraction studies of the as coated Thermal Barrier Coating System is presented. The results of the experiments conducted on the Kevlar® ballistic panels and the effects of matrix additives is detailed in Chapter 6. In Chapter 7 the conclusions and future outlook of these non-destructive testing methods will be discussed.

CHAPTER 2
PIEZOSPECTROSCOPY AND DIFFRACTION METHODS

2.1 Piezospectroscopy

Piezospectroscopy is a noninvasive technique that investigates changes in spectral response of the material with stress, under laser excitation. The molecular structure and constituents of the material may induce scattering or luminescence resulting in a characteristic optical spectra. Of particular focus for material study are two classes of piezospectroscopy, Vibrational and Photoluminescence spectroscopy. This research explores the techniques of Raman and Photoluminescence spectroscopy for the investigation of Thermal Barrier Coatings and advanced aerospace fiber composites. The ability to link the variations in spectral emissions captured by the techniques with the material's properties and resulting behavior allows for advanced material characterization and the determination of material response to realistic complex loading conditions.

2.1.1 Photoluminescence Spectroscopy

Photoluminescence Spectroscopy is an optical method of which an excitation source excites the electron cloud of a material resulting in the emission of new photons with a given wavelength. The excitation raises electrons to a higher energy state, and upon their return to the initial or ground state this results in the emission of photons. This

was originally described by the Rydberg formula in Equation 2.1

$$1/\lambda = R(1/n_1^2 - 1/n_2^2) \tag{2.1}$$

where λ represents the wavelength, R is the Rydberg constant, and n_1 and n_2 are integers with n_1 being the greater. [73]

In the case of α-alumina, Chromium^{3+} ions are present as a doping agent, either through material processing or through alloying. Even with trace concentrations, 0.01% the characteristic optical spectra for chromium doped alumina is observed.

The change in energy states due to excitation of the Chromium^{3+} ions for α phase alumina is presented in Figure 2.1 below.

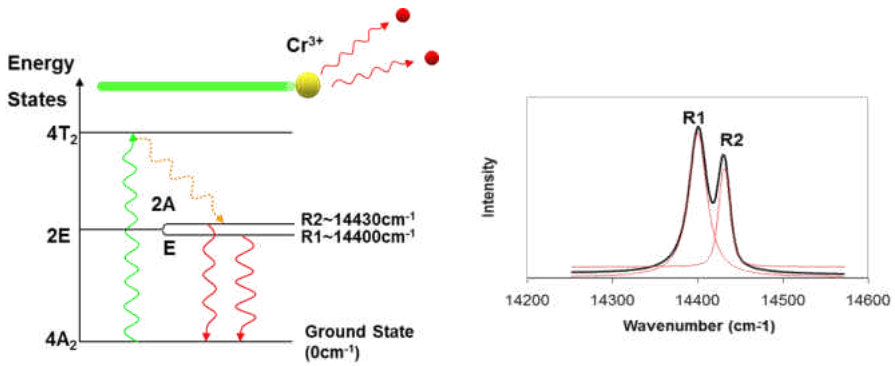

Figure 2.1: Photoluminescence Spectroscopy Theory Relating Excitation to Resulting Characteristic Optical Spectra

Photoluminescence spectroscopy is highly effective for investigating the thermally grown oxide in Thermal Barrier Coating systems coated by Electron Beam-Physical Va-

por Deposition method. By linking the optical phenomena with the material behavior mechanisms, the stress state, damage response, thermal response, and material composition can be investigated. [80, 136, 92, 117, 26, 52, 44] This potential has also initiated research in the development of this material as stress-sensitive embedded sensors with application in structural health monitoring for bridges, trusses, railroad tracks, aircraft joints, and other aerospace grade composites. [27, 121, 122]

2.1.2 Raman Spectroscopy

The second class of piezospectroscopy utilized in this study is vibrational piezospectroscopy. Raman Spectroscopy results from the atom or molecule scattering the excitation photons. In the process, the electron briefly jumps to an unstable virtual energy state due to the increased vibrational and rotational energy provided by the excitation. The electron falls to its original ground state, resulting in the characteristic spectra as a result of inelastic scattering and a reduction of energy. [127] This reduction of energy results in a change of wavelength. From this characteristic optical spectra, much information can be gleaned about the probed material. [6] An overview of this process is presented in Figure 2.2. Materials which have bonds that experience symmetric stretching or result in a change of polarizability indicates the material to be Raman active. [94]

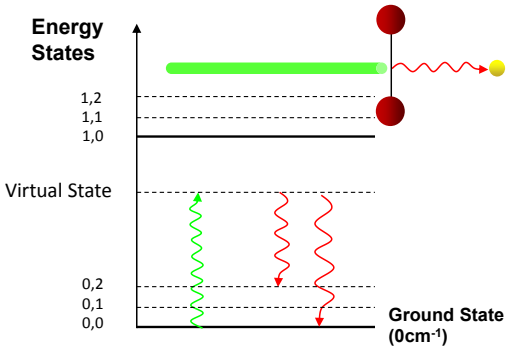

Figure 2.2: Raman Spectroscopy Theory Relating Excitation to Resulting Characteristic Optical Spectra

2.1.3 Collection Methods

In this work, a Princeton Instrument Acton Series 2150 spectrometer with a 1200 g/mm grating was attached to a fiber optic probe to collect piezospectroscopic readings. The Charged Coupling Device (CCD) resolution was approximately 20 μm per pixel. To calibrate, a Ne-Ar calibration source was utilized to match the observed spectra with the known reference spectra. A green 532 nm diode laser with approximately 18 mW of excitation power was used to conduct the piezospectroscopic studies. The resolved optical data was collected by the CCD and viewed through the accompanying LightField software.

2.1.4 Fitting Methods and Analysis

Pre-processing of the data was initiated to separate the map into discrete spectra for each measurement location. Following this separation process, the data was ready to be fit with a numerical equation. To facilitate the fitting and analysis of the piezospectroscopic data, an in-house gradient based pseudo-Voigt program was utilized with a least squares regression procedure. This analysis was performed using a Matlab-based algorithm. To fit the region of interest, the curves were truncated to include the doublet and the edge tails. Further, a linear baseline was removed to eliminate background fluorescence. To fit the characteristic doublet of α-alumina, two pseudo-Voigt were summed for fitting the convoluted peaks. Raman data was fit with a similar program utilizing a pseudo-Voigt function with least squares regression.

Upon arriving at a good initial approximation, the raw data was then fit with the numerical approximation. The fit peaks were then brought to the mapping program which generated high resolution contour maps of the fit peak location, the deviation from a zero stress reference peak, and the resulting stress profile.

2.2 Synchrotron Radiation

Synchrotron Radiation has been used for material characterization due to its high energy affording throughput transmission and Angstrom scaled resolution. Further the through

transmission diffraction method is preferred, as high energy X-rays are biased for smaller angles and reflection would reduce the sampled depth. [72, 128, 135] High energy X-Ray diffraction can be employed for studying several material properties and responses. These include phase identification, grain size, strain profiles, crystallographic changes, and thermal expansion. [116, 120, 123, 114, 139, 86]

2.2.1 X-Ray Diffraction Techniques

An overview of the fundamentals of Strain Analysis is presented in Figure 2.3. In Figure 2.3A, an overview of a synchrotron X-Ray source is detailed. X-Rays are generated through a linear accelerator with supporting booster ring. Photons are collected in the lengthy storage ring before being accessed by the user by a bending magnet or insertion device. In Figure 2.3B the principle behind Bragg‘s Law is shown. Braggs Law expresses the governing equation of the scattering of photons due to a crystal lattice. This scattering is due to the nature of photons being deflected by the charged electron cloud, and passing through the keyhole lattice spacing of the crystallographic planes. [28] Bragg‘s Law is presented in Equation 2.2.

$$2dsin(\theta) = n/\lambda \tag{2.2}$$

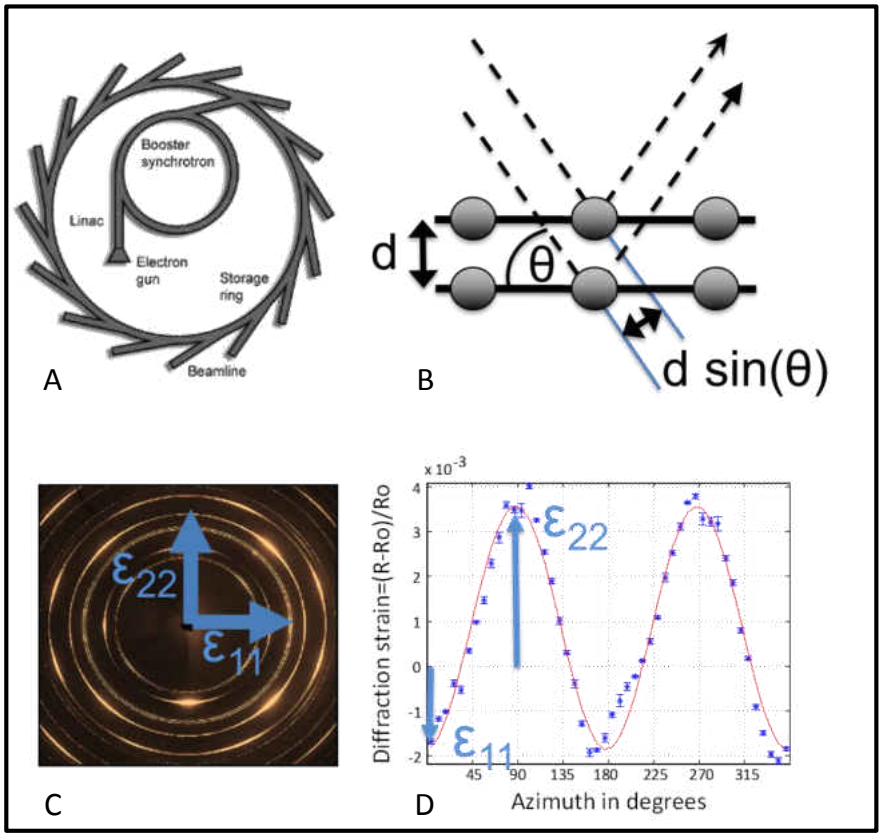

Figure 2.3: Fundamentals of X-Ray Diffraction: A) Schematic of Synchrotron Light Source B) Bragg's Law Relating Crystalline Planes to Diffraction Angle C) Debye-Scherrer Rings Collected by a 2D Area Detector D) Strain Curve Fit for a Single Measurement

Also represented in Figure 2.3C, is an example of the collected Debye-Scherrer rings which result from diffraction. The rings are a 2 dimensional slice of the diffracting cone of exiting X-Rays. X-Ray diffraction strain analysis is conducted by measuring the deviation of the ring from a perfect circular ring. This eccentricity corresponds with the principal strains, ϵ_{11} and ϵ_{22} as indicated on the set of rings. Figure 2.3D shows a representative

strain profile for a measured ring, with the corresponding ϵ_{11} and ϵ_{22} deviating the strain curve from the zero position.

2.2.2 Collection Methods

X-Ray diffraction experiments were conducted at the Advanced Photon Source at Argonne National Laboratory at the 1-ID beamline in Sector 1. The high energy X-Rays were tuned to 65 keV and applied via insertion device. This energy corresponds to a minimum diffraction ring available for collection of 1.29 Å. The beam was initialized to graze the surface of the tubular geometry and moved inward towards the center of the sample to map the strain distribution throughout the respective layers as shown in Figure 2.4. The focus of this study is on the grazing method only, as it minimized the depth of the diffraction volume and reduced doublet and broadening effects due to the complex geometry.

The investigation used a 2D GE detector with a pixel size of 200μm and Huber goniometers. The beam step size was held at 30μm and a window size of 30 by 300μm.

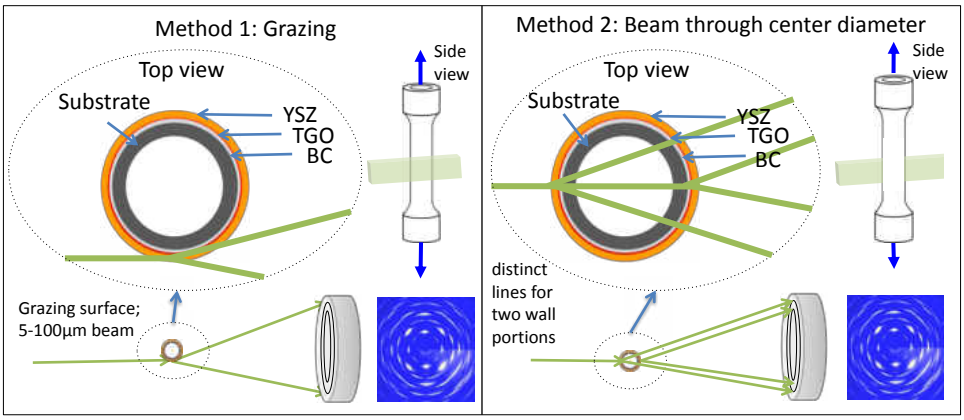

Figure 2.4: Method 1: Grazing surface from 5 to 100 μm. 2D detector measures axial and radial components of strain. By moving the sample into the beam, each layer can be scanned and collected. Method 2: Direct transmission along center line. 2D detector measures wall-thickness averaged axial and circumferential components of strain. [114]

2.2.3 Fitting Methods and Analysis Procedures

The collected Debye-Scherrer Rings as presented in Figure 2.3C, are integrated azimuthally into a transformed line. The deviation from center is indicative of strain present in the phase under examination. [49]

The transform plot is then divided into discrete bins, of which the radial position of the intensity is then plotted and fit using a pseudo-Voigt routine in Matlab. The variation between the fit radial positions of the intensity in each azimuthal bin is then fit to the strain equation. [1]. This is described in Figure 2.5.

In Figure 2.5A, the plotted transform for NiAl peak (110) is presented. This transform is then discretized into radial bins for fitting as seen in Figure 2.5B. The resulting intensity fit from each bin is then input into the strain equation, which results in the measurement's strain profile.

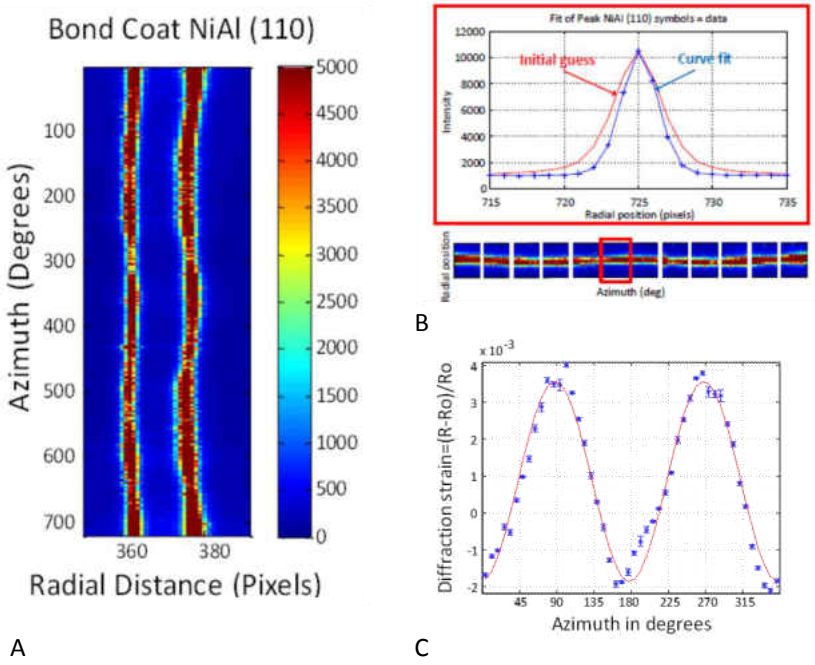

Figure 2.5: Strain Fitting Procedure: A) Transformed Lineout Plot Around Azimuth B) Discretized Transform Bin for Fitting C) Fit Strain Curve

CHAPTER 3
SPECIMEN MATERIALS, GEOMETRY, AND EXPERIMENTAL SETUP

The design of samples and techniques used for piezospectroscopic and diffraction measurements for thermal barrier coatings and fiber composites is discussed herein.

3.1 Thermal Barrier Coating System

To best understand the material behavior and damage mechanics of thermal barrier coatings, the experiment was designed to include a complex geometry and representative service loads. This section will discuss the design and methodology of the study on Thermal Barrier Coatings.

3.1.1 Sample Design

The Thermal Barrier Coating System that was designed for this study's experiments was comprised of an Inconel 100 superalloy substrate with a 7% Yttria partially stabilized Zirconia adhered to the substrate via a NiCoCrAlY bond coat. The deposition method was Electron Beam-Physical Vapor Deposition for both the bond coat and the top coat, which produces a columnar structure in the YSZ top coat. A thin thermally grown oxide layer forms during the coating process, and is estimated to be 0.5 μm for our sample. A representation of this system is presented in Figure 3.1.

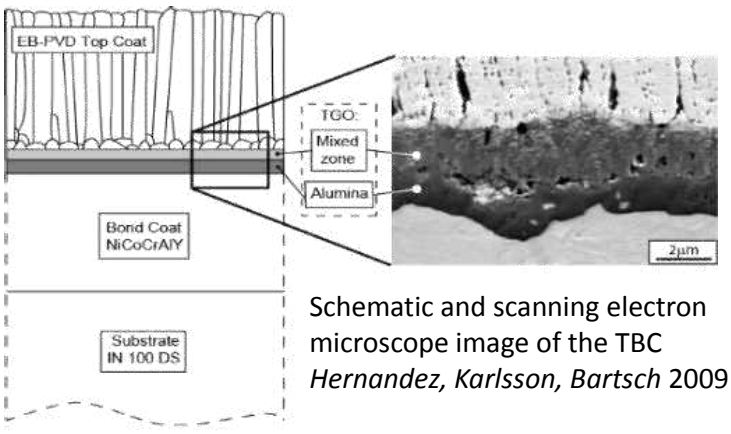

Figure 3.1: Thermal Barrier Coating System

[60]

The specimen was designed with a tubular geometry of inner diameter 4 mm and outer diameter 8 mm. Electron Beam-Physical Vapor Deposition was used to create the top and bond coats to a thickness of 240 μm and 80 μm respectively. The coated length was 102 mm of the full length of 160 mm. The geometry is presented in Figure 3.2.

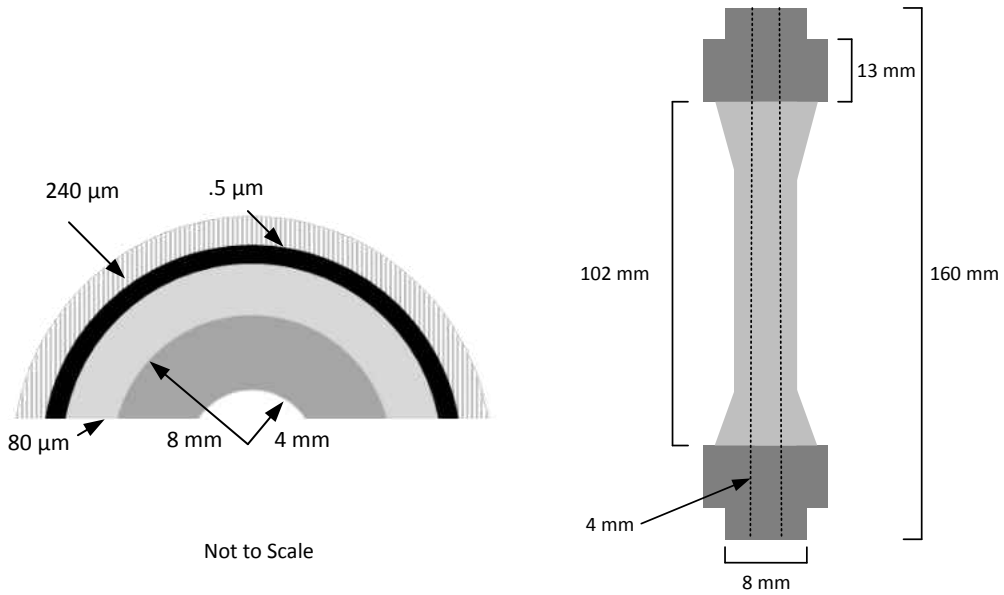

Figure 3.2: As Coated Sample CAD

Sample design and manufacturing took place at the German Aerospace Center (DLR) in Cologne, Germany. For the manufacture of coatings, the institute runs two EB-PVD coaters; one single source 60kW Leybold coater and one von Ardenne 150kW two-source coater.

Figure 3.3: As Coated TBC Specimen

The as-coated specimen is presented in Figure 3.3. The specimen was additionally threaded for testing under tensile mechanical loading.

3.1.2 Material Properties

The mechanical and material properties known for the Thermal Barrier Coating system are presented in Table 3.1.

Table 3.1: High Temperature and Room Temperature Material Properties for Thermal Barrier Coating System on IN100 Substrate [60]

	Substrate		Bond Coat		TGO		Top Coat	
	RT	HT	RT	HT	RT	HT	RT	HT
Elastic modulus, radial[GPa]	215.00	148.00	140.00	70.00	360.00	340.00	13.00	16.00
Elastic modulus, axial [GPa]	120.00	80.00	-	-	-	-	-	-
Poisson ratio, ν	0.30	0.30	0.32	0.35	0.24	0.24	0.22	0.28
CTE, $\alpha[10^{-6}1/K]$	11.50	18.80	8.60	16.60	6.00	8.70	9.00	11.50
Thermal Cond.,$\lambda[W/mK]$	15.00	30.00	8.70	27.50	23.00	5.00	1.88	1.60
Density, $\rho[g/cm^3]$	7.75	7.29	7.80	7.43	4.00	4.00	5.00	4.84
Heat capacity, Cp [J/kgK]	400.00	580.00	390.00	700.00	769.00	1261.00	500.00	630.00

Table 3.1 presents data showing that the room temperature properties are considerably different than the properties at high temperature. This is critical, particularly in the thermal expansion mismatch, and drives the high strains in the thermally grown oxide.

3.1.3 Experimental Design, Loading Conditions, and Measurement Methods for the Study of Thermal Barrier Coatings

The specifications regarding the experimental design for the Thermal Barrier Coating System are detailed herein. Three loading conditions were investigated in three different material states, including: the as-coated specimen, the early cycled specimen, and the long duration aged specimen.

3.1.3.1 Design of Experiments for Thermal Gradient and Mechanical Loading for an As-Coated Specimen by Methods of X-Ray Diffraction

The as-coated specimen was designed for application of tensile mechanical loading, thermal loads, and induced internal cooling by the inflow of compressed ambient air through the internal chamber. Mechanical loads were designed for a range of 16-128 MPa to accompany the thermal loading. The exterior surface temperature was held at 1000 °C and ensured by encircling the specimen with a 0.35 mm type S thermocouple comprised of Platinum-Rhodium (90%-10%) alloy and pure Platinum. The thermocouple was used in a feedback loop to precisely hold the exterior of the sample. The sample was contained in an infrared chamber heater manufactured by Precision Controls of Research INC., which delivered 8 kW of power via 4 quartz lamps focused on the center line by reflecting mirrors.

Induced cooling was regulated by an Omega mass flow controller FMA5400/5500 from 0-100 standard liters per minute (SLPM). To facilitate mechanical loading, superalloy grips were designed to hold and impart load in line with the servohydraulic mechanical load frame. These grips were placed partly in the heating chamber and as such had to handle high thermal loads. This challenge was surmounted by using Inconel 718 for the grip material. Type K thermocouples were placed on the top and bottom grips to ensure the integrity of the connection and to identify the amount of conduction taking place

away from the sample. A schematic representation of the loading conditions is presented in Figure 3.4 and Figure 3.5.

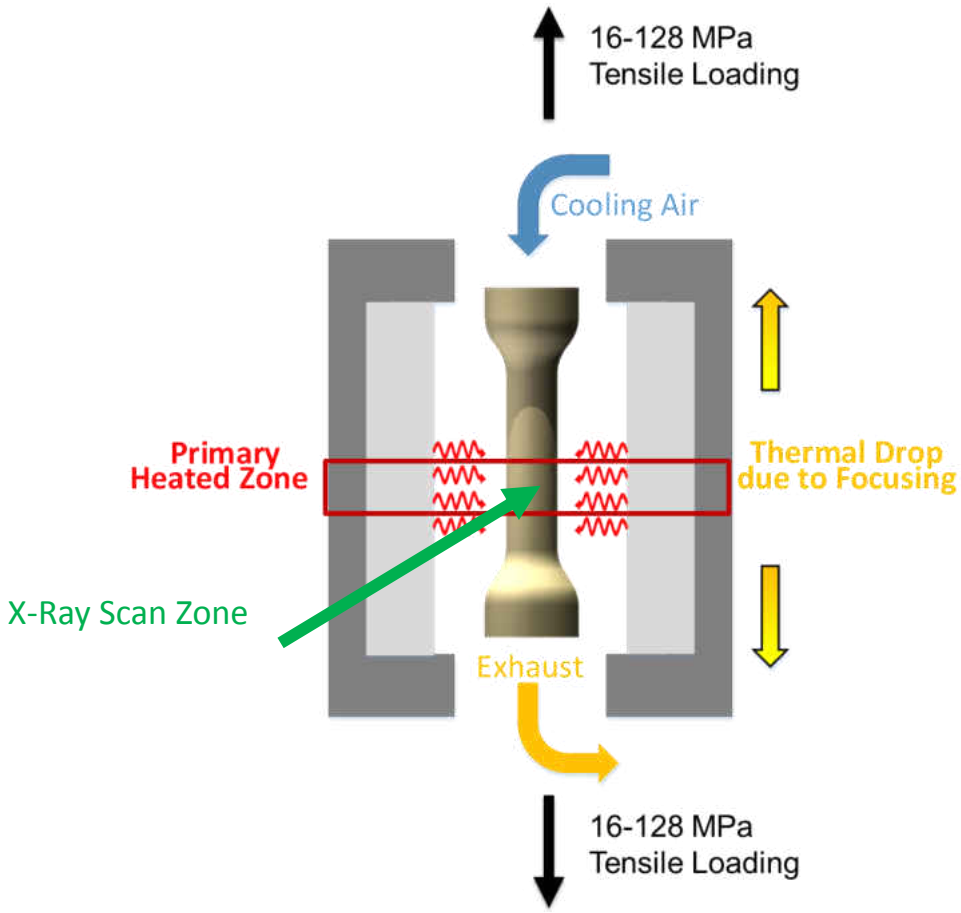

Figure 3.4: Design and Description of Loading Conditions for in-situ X-Ray Diffraction Study

X-Ray diffraction measurements were conducted at the center of the gauge section in an area assumed to be near uniform in thermal loading. A schematic representation is presented in Figure 3.5 .

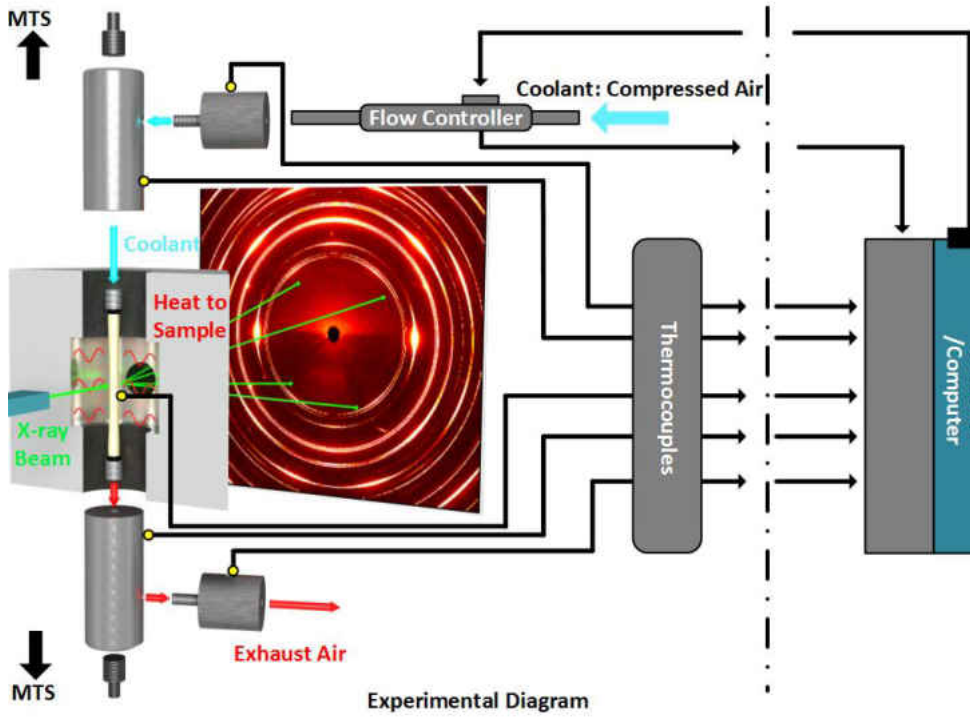

Figure 3.5: Design of Thermal Gradient and Mechanical Loading for X-Ray Diffraction Measurements

Specifications regarding the design and setup of the in-situ measurement apparatus can be found in the accompanying publication. [114] The X-Ray diffraction study took a 10 file depth-scan with the grazing technique, with a 30 μm step. The data was collected at 5 frames per measurement, with an exposure time of 0.5 seconds per frame. This was

done for a representative loading cycle showcased in Figure 3.6, with a high temperature hold at 1000 °C for 40 minutes and 20 minute ramp times. The associated thermal data was also collected from the various thermocouples in the system. Mechanical, thermal, and flow-rate data was collected for ancillary measurements to accompany the X-Ray diffraction data.

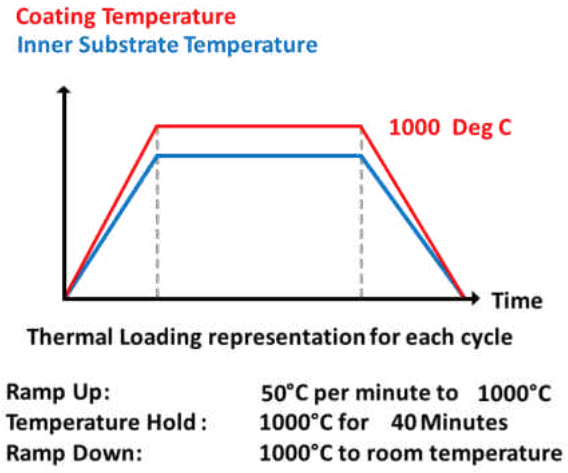

Figure 3.6: Representative Thermal Cycle

The discretized bins for the scan through the coating layers is presented in Figure 3.7. Due to the nature of the cylindrical geometry, zirconia was always present in the diffraction data as the measurement scanned inward towards the sample center.

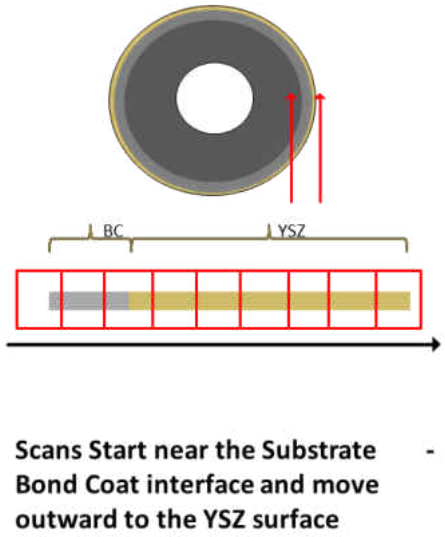

Figure 3.7: Scanning Window for X-Ray Diffraction

3.1.3.2 Design of Experiments for an Early Cycle Specimen by Means of Piezospectroscopy

Early cycling was a byproduct of the tests conducted on the as-coated specimen. The test consisted of 17 cycles at high temperature. The Thermally Grown Oxide develops quickly and non-linearly during its early development before slowing, as TGO growth is dominated by oxygen diffusion through the thin layer. [60, 4, 131, 105] The loading conditions imparted on the specimen were varied including the mechanical load from 16-

128 MPa and induced cooling from 0-100 SLPM. This resulted in a maximum gradient of 140 °C thermal drop over the 240 μm zirconia top coat, which compared well with literature [109]. Further, the surface temperature at the center of the gauge section was ramped from ambient to high temperature and held at 1000 °C. Due to the nature of the furnace's focusing, a thermal gradient was expected to be present in the vertical axis, which was further intensified by the incoming cooling air imposed on the center of the tubular specimen. As the ambient air flowed through the top grip and passed through the specimen's heated length, the rate of convective heat transfer was not expected to be constant. This was confirmed by the thermocouples located on the grips and in the inlet and exit flow. While the measurement location for the X-Ray diffraction study was constrained in the near uniform loading condition window, observations on the early cycled specimen will be conducted to map these variations. This will allow the investigation of the predicted outcome, that for early cycled specimen's oxide growth is highly dependent on the imposed loading conditions. An image from the in-situ diffraction measurements resulting in early cyclic is presented in Figure 3.8. These loading conditions developed the residual stress state for the material to be investigated.

Figure 3.8: Specimen in Thermal Gradient and Mechanical Loading Apparatus

Due to the 17 thermal cycles imposed on the specimen, the TGO growth is expected to have resulted in an increase in the thickness of the thin layer to approximately 1.5 μm. The thickness approximation was determined from a growth model developed in literature. [60] This growth is localized, while the rest of the coating layers maintained their original thickness. A schematic of this is presented in Figure 3.9.

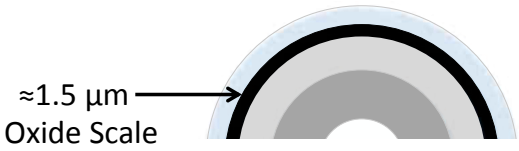

Figure 3.9: Estimated TGO Thickness after 17 Cycles

For the specimen under early cycling, piezospectroscopic measurements were conducted to develop a stress profile for the thermally grown oxide layer and the ceramic top coat. To conduct these measurements, a green 532 nm diode laser with 19 mW of power was utilized to excite a piezospectroscopic response. An exposure time of 4 seconds was used to optimize the collection. Calibration was conducted with a Neon-Argon source lamp. For Face A, as referred to in Figure 3.10, the calibration produced an expected uncertainty of $\pm 0.030\ nm$ Root Mean Square (RMS), and 0.028 nm RMS for Faces B, C, and D $\pm$. A Princeton Instrument Acton Series 2150 spectrometer with a 1200 g/mm grating was utilized by way of a fiber optic probe to collect the piezospectroscopic data. An image of the setup is presented in Figure 3.11.

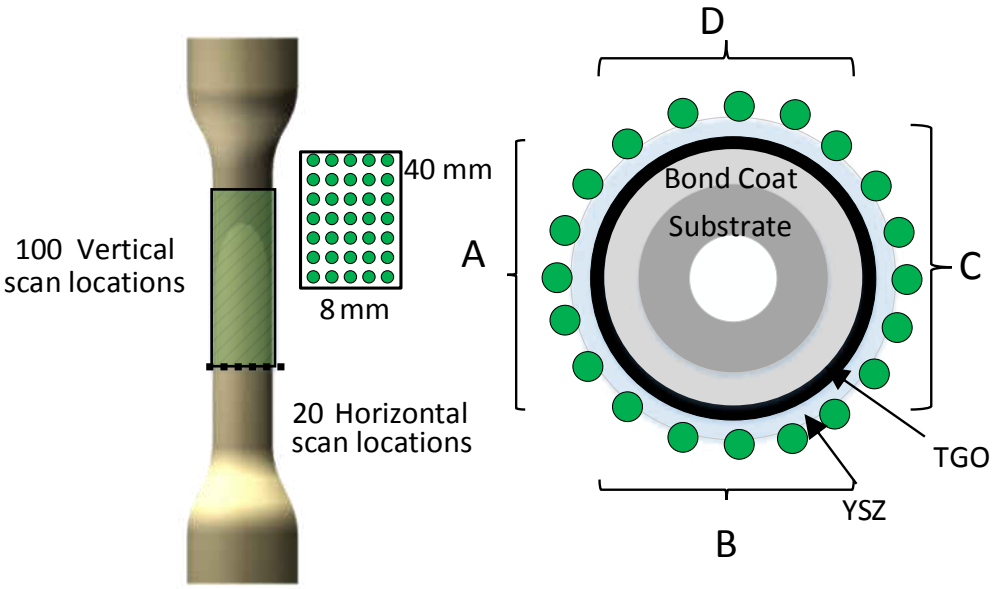

Figure 3.10: Piezospectroscopic Scanning Zones

For the early developing oxide, four snake scans of 2000 points each were collected to produce a high resolution map. The resolution in the vertical and horizontal scan direction measured 400 μm, with 100 vertical scan rows and 20 horizontal scan columns. This covered an area of 40 mm by 8 mm. Each scan was turned 90 $^\circ$ which provided 360 degrees of overlapping data. The portable spectrometer setup is presented in Figure 3.11.

Figure 3.11: Portable Spectrometer for Piezospectroscopic Measurements.

The ceramic top coat was scanned with similar methodology, but under a less resolute scan of 40 vertical scan rows and 6 horizontal scan columns. An exposure time of 2 seconds was used to optimize the collection and avoid saturation. The resolution in the vertical and horizontal scan directions measured 800 μm. Slight overlap was provided as each scan covered 4.8 mm across and 32 mm in the vertical.

The scan was focused on the midsection of the primary heated zone and upward to the top of sample. This was designed to measure the regions of variation induced by slight changes in thermal loading and interactions with the induced cooling flow on the inner wall of the tubular sample. Results of the measurement on the early cycle specimen are presented in Chapter 4.

3.1.3.3 Design of Experiments for a Specimen Following Long Duration Aging

Following testing on the early cycled specimen, the specimen was sent to the DLR in Cologne, Germany where it was placed in a furnace for long duration aging. The aging was conducted at 1000 °C with zero mechanical load and no induced cooling. Each day the specimen was removed from the furnace to check for visible spallation damage, effectively cycling it. The aging was conducted for a total of 264 additional hours at high temperature. The TGO layer is expected to be approximately 3.75μm [60]. This aging process more than doubled the thickness of the TGO, resulting in a marked effect of the system's stress profile. These loading conditions introduced a change in the residual stress state for the material to be investigated.

After 264 hours of thermal aging on the specimen, piezospectroscopic measurements were conducted to develop a stress profile for the thermally grown oxide layer and the ceramic top coat, and to investigate any signs of damage due to the prolonged time at temperature. To conduct these measurements, a green 532 nm diode laser with 19 mW of power was utilized to excite a piezospectroscopic response. An exposure time of 3 seconds was used to optimize the collection. Calibration was conducted with a Neon-Argon source lamp. As referred to in Figure 3.12, the calibration produced an expected uncertainty of 0.029 nm RMS for Faces A, B, C, and D ±. A Princeton Instrument Acton Series 2150 spectrometer with a 1200 g/mm grating was utilized by way of a fiber

optic probe to collect the piezospectroscopic data. An image of the setup is presented in Figure 3.11. For the aged specimen's oxide scale, again four snake scans of 2000 points each were collected to produce a high resolution map. The resolution in the vertical and horizontal scan direction measured 400 μm, with 100 vertical scan rows and 20 horizontal scan columns. This covered an area of 40 mm by 8 mm. Each scan was turned 90 $^\circ$ which provided 360 degrees of overlapping data.

The ceramic top coat was scanned with similar methodology to that for the oxide scale, but under a less resolute scan. The scan increased to 50 vertical scan rows and 6 horizontal scan columns, to match the vertical depth of scan afforded to the thermally grown oxide. An exposure time of 3 seconds was used to optimize the collection. The resolution in both the vertical and horizontal scan direction measured 800 μm. Slight overlap was provided as each scan covered 4.8 mm across and 40 mm in the vertical. This methodology was used to be able to showcase the variation from long duration aging.

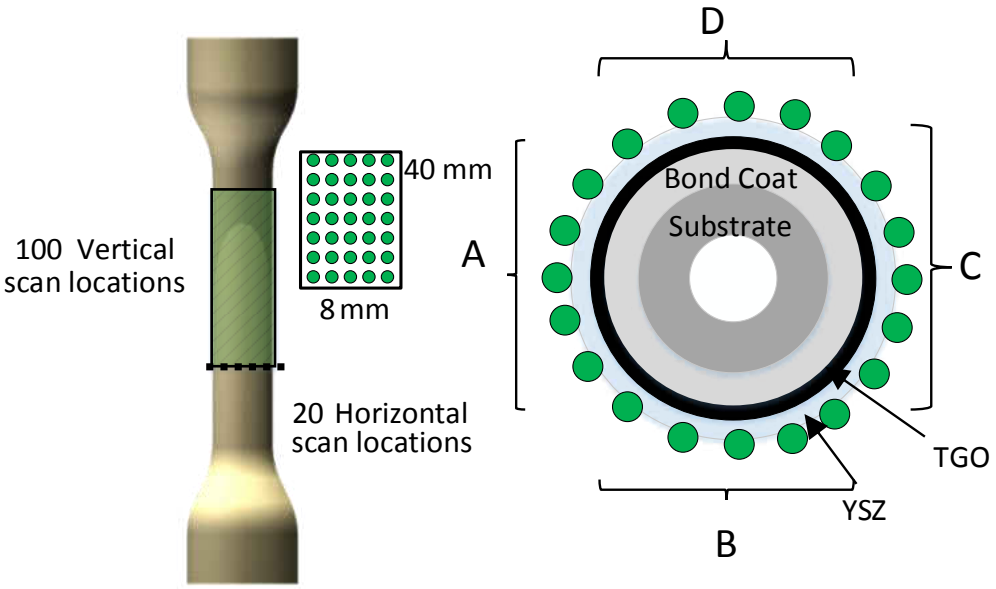

Figure 3.12: Piezospectroscopic Scanning Zones for Aged Specimen

Similar to the early cycle specimen, the scan was focused on the midsection of the primary heated zone and upward to the top of sample. This was designed to measure the regions of variation induced by subtle changes in the thermal loading, and interactions from the induced cooling flow on the inner wall of the tubular sample. Results of the measurements are presented in Chapter 4.

3.2 Kevlar® Ballistic Panels

Kevlar® composites have a wide range of application in both defense and commercial industries. These applications, including ballistic armor and shielding, require balancing weight minimization to the added strength afforded by the composite. These composites allow for energy to be absorbed and deflected through elongation of the polymer fibers as well as delamination in system with multiple stacked layers. [5, 20] These Kevlar® composites are commonly used due to their excellent strength to weight ratio, and their ability to absorb a high degree of impact, even from ballistics.

Developing the ability to accurately model both the impact of ballistic materials, as well as the response and behavior of the fiber composites, is of high importance to current research. Understanding how the force and subsequent damage is propagating will allow for the development of more robust composites. [30, 41, 99] The impact causes stress contours which elongate the weave, dissipating energy.

3.2.1 Sample Design

Kevlar® 29 is a polymer chain of Poly-paraphenylene terephthalamide, produced by the reaction of para-phenylenediamine and terephthaloyl chloride. During manufacturing, the fibers are pulled, thereby orienting the polymer chains in the loading direction. Commonly the fibers are spun yielding very high tensile strength. [103, 132, 43] The

polymer chain is presented in Figure 3.13, with a single chain denoted in bold. The polymer chains are compiled into thin sheets, which are combined in a radial fashion to form a cylindrical Kevlar® Fiber. This build up, as well as a sample of the pristine fiber weave, are presented in Figure 3.13.

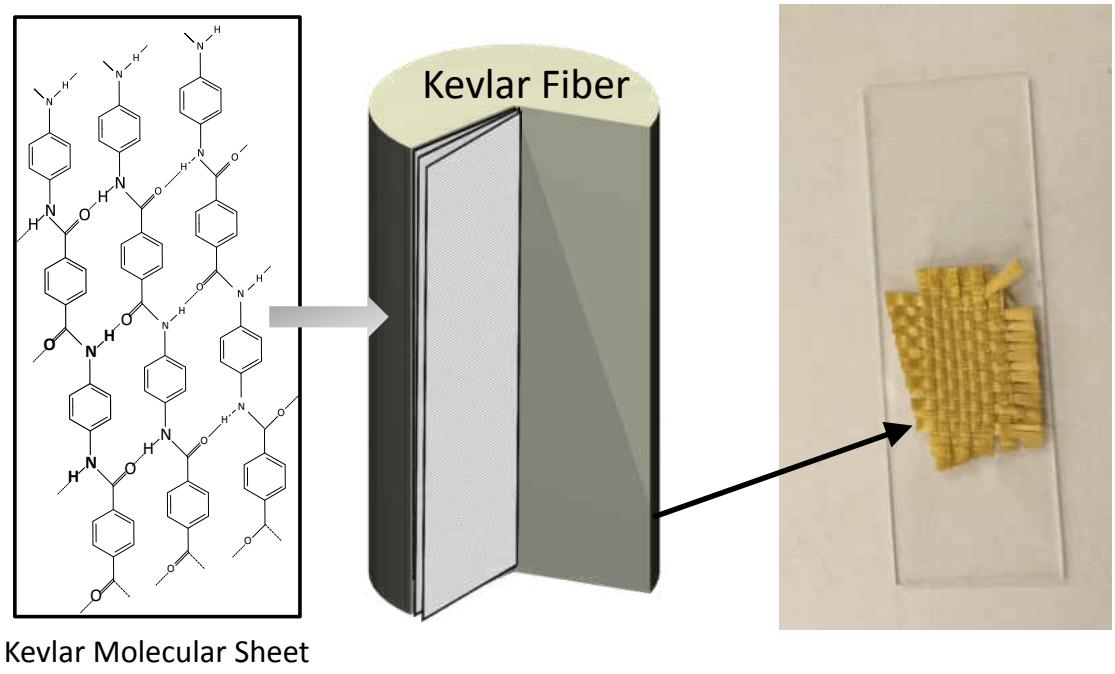

Figure 3.13: Molecular Structure of Kevlar® (Left), its Orientation in a Kevlar® Fiber (Center), and Pristine Weave (Right)

3.2.2 Material Properties

Table 3.2: Material and Mechanical Properties of Kevlar® 29 and Kevlar® 49 [43]

	Spec. Density [lb/in^{-3}]	**Tenacity [10^3 psi]**	**Modulus [10^{-6} psi]**	**Break Elong.%**	**Spec. Tensile Strength [10^6]**	**CTE [10^6/F]**	**Decomp. Temp. [F]**
Kevlar 29	0.052	424	10.2	3.6	8.15	-2.2	800-900
Kevlar 49	0.052	435	16.3	2.4	8.37	-2.7	800-900

In Table 3.2, the material and mechanical properties for both Kevlar® 29 and Kevlar® 49 are presented. This study is focused on Kevlar® 29 which has application in body armor and ballistic resistant panels, though the analysis techniques are applicable for both composites.

Table 3.3: Kevlar® 29 Raman Properties, Theoretical vs. Experimental Results [20, 69, 101, 134]

Theoretical (cm^{-1})		**Experimental (cm^{-1})**					
Penn & Milanovich, Kim et al.		Washer, Brooks and Saulsberry					Cen et al.
		Kevlar® Yarn	**Kevlar® Strand**				
		647 nm	488 nm	647 nm	752 nm	1,064 nm	633 nm
1,615	1,615	1,613	1,612	1,613	1,612	1,615	1,611
1,649	1,654	1,649	1,649	1,649	1,649	1,651	–

3.2.2.1 Baseline Fiber Composite

The pristine Kevlar® fibers are woven before impregnation with an epoxy resin. The baseline Kevlar® composite panel used in this study was developed with Rhino Epoxy

1403 bisphenol-A, with a cycloaliphatic amine hardener. The manufacturing was conducted in Dr. Jihua Gou's research facility at The University of Central Florida. The manufacturing utilized a Binks 18" impregnation machine, coupled with pinch rollers. An image of the baseline fibers via scanning electron microscopy is presented in Figure 3.14.

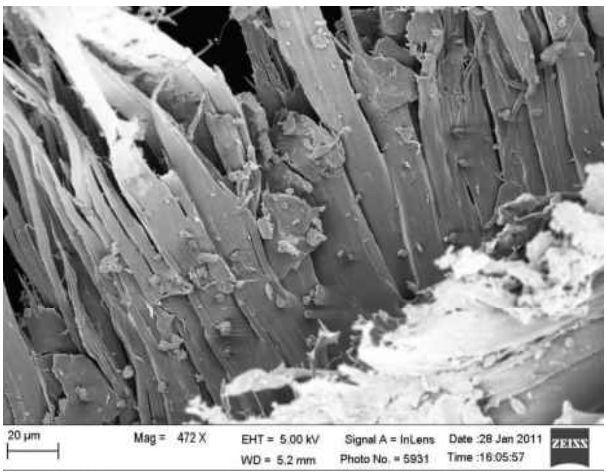

Figure 3.14: Scanning Electron Microscopy of Baseline Kevlar® Composite [51]. *Image Credit*: *Jason Gibson*

The composite was then cured in an autoclave. The final product was formed into ballistic resistant panels with dimensions of 18 inches by 18 inches with a depth of 0.310 inches as seen in Figure 3.15. The panels were comprised of 16 distinct plies of the fiber weave with impregnated matrix.

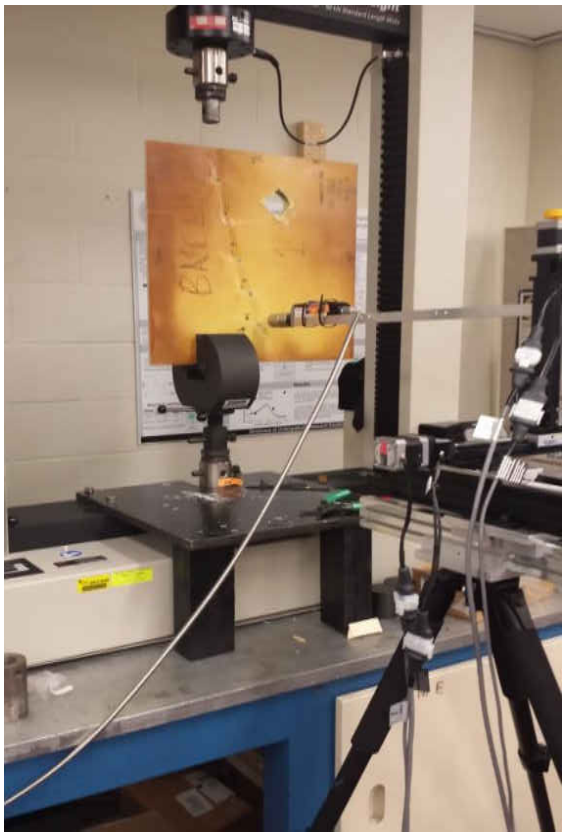

Figure 3.15: Baseline Kevlar® 29 Panel Composite

3.2.2.2 Matrix Additives

To enhance the material strength and ballistic resistance performance of the composite, two classes of additives were considered. This study utilized customized Kevlar® composites, with one doped with multi-walled carbon nanotubes (MWCNT) and another with core shell rubber particles (CSR) in conjunction with the baseline Kevlar® fiber

weave and epoxy matrix. The Graphistrength® nanotubes were supplied by Arkema and were dispersed at 25% concentration. An image of the nanotubes embedded in the composite via scanning electron microscopy is presented in Figure 3.16. The diameter and lengths were approximately 100 nm and 100 μm respectively. Material properties provided detailed a specific gravity of 2.90 g/cm^3 and a tensile modulus of approximately 103 GPa. Kane Ace Core® shell rubber particles were produced by Kaneka and dispersed into the baseline epoxy matrix a concentration of 33%. Particle spheres had approximately a 100nm diameter. An image of the nanoparticles dispersed in the matrix via tunneling electron microscopy is presented in Figure 3.17.

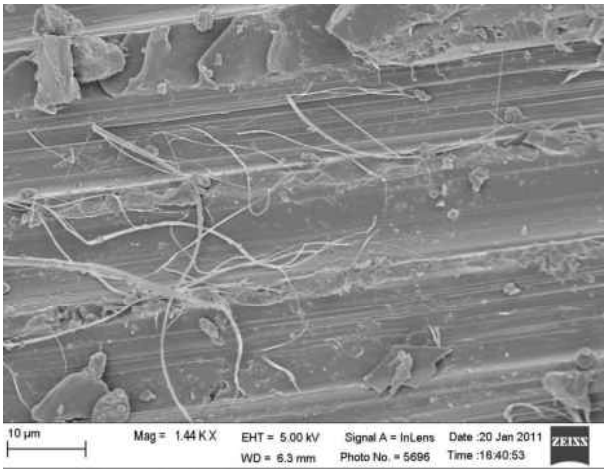

Figure 3.16: Scanning Electron Microscopy of CNT Additive to Kevlar® Composite [51]. *Image Credit*: *Jason Gibson*

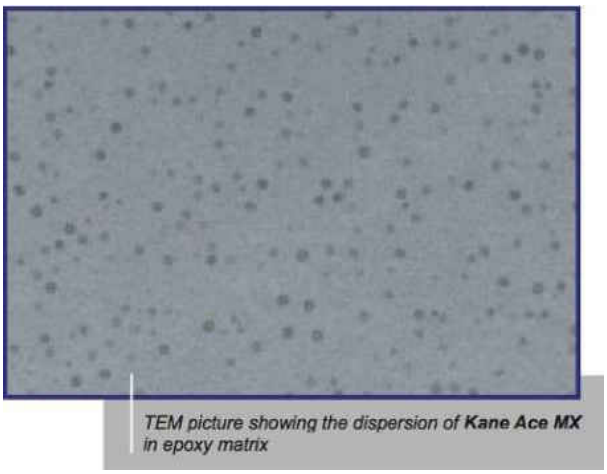

Figure 3.17: Tunneling Electron Microscopy of CSR Kevlar® Composite [51]. *Image Credit*: *Jason Gibson*

The final product was formed into ballistic resistant panels with dimensions of 18 inches by 18 inches as seen in Figure 3.18. The CNT panel is presented in Figure 3.18A and the CSR panel is presented in Figure 3.18B.

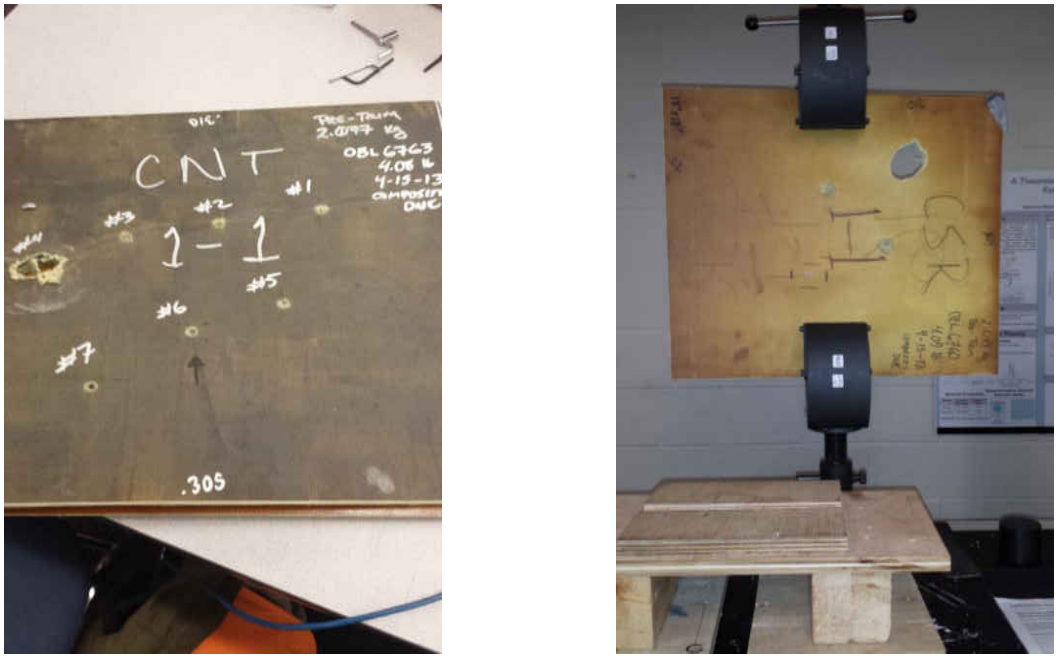

Figure 3.18: A) Carbon Nanotube Additive Panel and B) Core Polymer Ball Additive Panel

3.2.3 Experimental Design, Loading Conditions, and Measurement Methods for Kevlar® Composites

The Kevlar® ballistic baseline and additive panels were tested with a high velocity ballistic round. The testing utilized a .44 Mag 240 grain Semi-Wadcutter Gas Check

(SWCGC) bullet from a universal barrel holder with a 10 inch 1:20 barrel. The panels were received for piezospectroscopic study after the conclusion of the colleagues' ballistic study. The post shot condition was then to be analyzed for the imparted residual stress state around the bullet entrance and exit sites.

To scan the Kevlar® ballistic samples, Raman spectroscopy was conducted. For the baseline panel, a 6x6 map was measured encompassing the hole with a scanning area of approximately 25x25 mm. The scanning region is presented in Figure 3.19. A Renishaw RM-1000 Ramascope with a 1800 groove/mm grating was employed by way of a fiber optic probe with a 50x Nikon objective. A green 532 nm diode laser with 9 mW of power was utilized to excite a Raman response. Measurements were conducted following calibration of the equipment with crystalline silicon, which has a sharp and well research Raman band peak at 520 cm^{-1} of high intensity. A total of 36 data points were collected of varying intensity and noise. Measurements conducted on the edge of the sample were delineated to see the variance of the scanned region closer to the bullet.

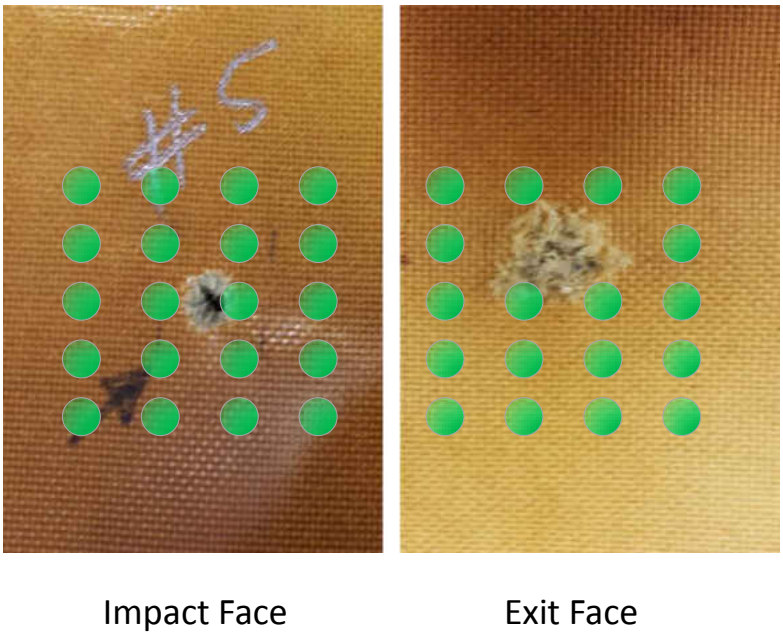

Figure 3.19: Mapping Routine for Ballistic Damage for Kevlar® Panels

For the additive panels, collection of Raman spectra was considerably more challenging. The additives present in the matrix showcased a great deal of background fluorescence, particularly from the CSR polymer balls. As such small, tightly packed scans of 8 points were collected sufficiently away from the bullet hole to identify the residual stress effects. Continuing to perfect the scanning techniques is continuing in the future work, in an effort to develop complete contour maps of the impact region. This modified scanning path is presented in Figure 3.20. Results of the measurements are presented in Chapter 6.

Figure 3.20: Limitations in Scanning

CHAPTER 4
PIEZOSPECTROSCOPIC STUDY OF THERMAL BARRIER COATING SYSTEMS

4.1 Objectives

The objectives for the piezospectroscopic studies on the Thermal Barrier Coating System were as follows. The primary objective was to collect piezospectroscopic data from the thermally grown oxide layer and ceramic top coat, for an early cyclic aged specimen with complex tubular geometry. The second objective was to identify variations in thermal loading and their influence on system's development ex-situ. Further objectives included resolving a high resolution stress map of the thermally grown oxide and ceramic top coat. A comparison of the specimen after early cyclic aging and long duration aging is also for investigation, to identify variations in the stress field and damage associated with prolonged exposure at high temperatures. A representation of the studies on the specimen and the resulting optical spectra for analysis is presented in Figure 4.1.

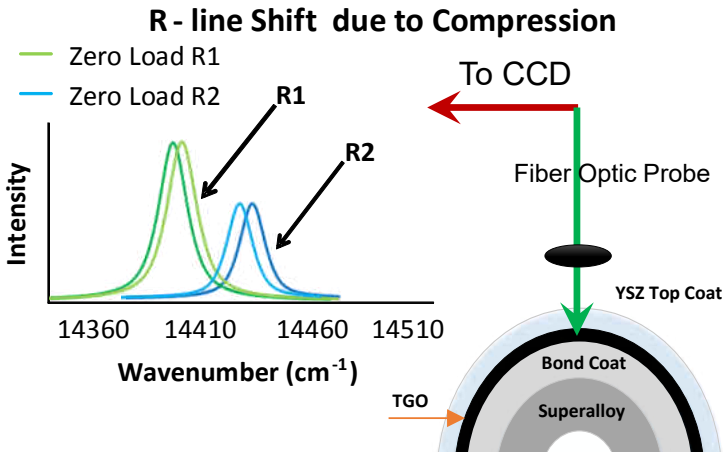

Figure 4.1: Scanning Schematic for Conducting Photoluminescence on Thermally Grown Oxide and the Optical Spectra Collected

4.2 Photoluminescence of Thermally Grown Oxide From Early Cyclic Aging

The results from the piezospectroscopic studies on the Thermal Barrier Coating System are presented herein. Initial scans of the thermally grown oxide revealed the characteristic optical spectra of α-alumina on the CCD. The finding is presented in Figure 4.2. The clear and distinct doublet peak is present and is consistent with the expected photoluminescence of the material at 14,403 cm^{-1}, approximately 633 nm. It can be noted from the profile that the scan was completed in the absence of the majority of ambient light to minimize noise in the data.

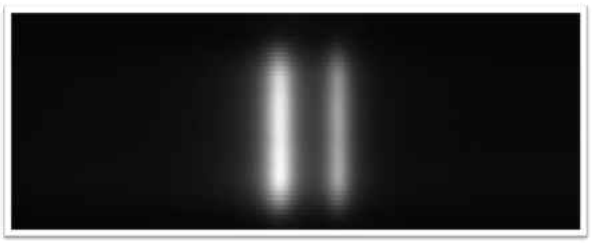

Figure 4.2: Collected Optical Spectra on CCD

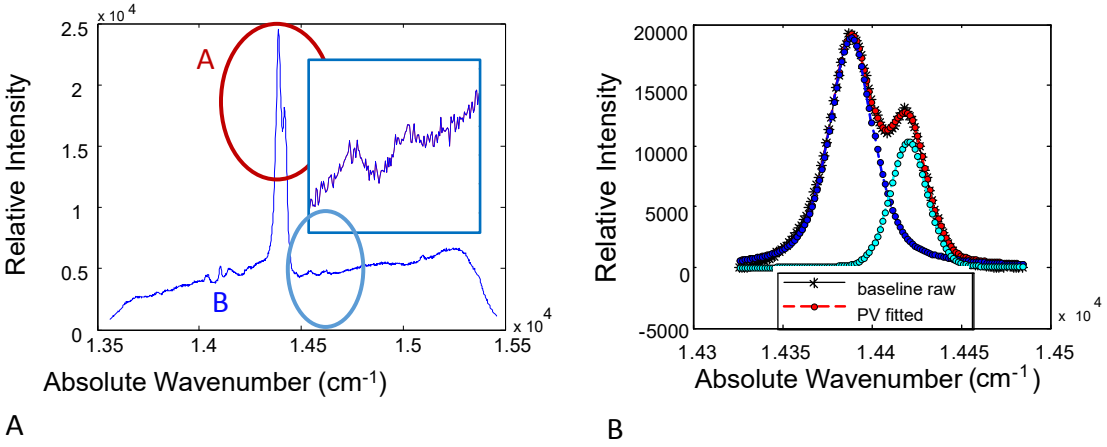

Figure 4.3: A) Optical Spectra of Thermally Grown Oxide with Phase Identification B) Fitted Doublet Peak for α-Phase Alumina

The collected spectra has been plotted in Figure 4.3. In Figure 4.3A, the characteristic doublet of α-alumina is observed and marked in the highlighted region A. Further, trace concentrations of θ-alumina were identified in highlighted region B by the characteristic doublet at approximately 14,550 cm^{-1} and 14,620 cm^{-1}. This was comparable with

literature [133], with the peak spacing approximately at 70 cm^{-1}. The peak shift was similar to that of the α phase, suggesting both phases are under a high compressive stress.

In Figure 4.3B, a measurement of an the α-phase doublet after the fitting procedure is presented. The resolved peaks are approximately 14,387 cm^{-1} and 14419 cm^{-1}. This value is a shift from the known reference of 14,403 cm^{-1} and 14,433 cm^{-1} for stress free α-alumina [11, 63]

Having collected the optical spectra for each map, the next aim was to convert the change in wavenumber as seen in Figure 4.4A to its corresponding stress value. This is done by using the Piezospectroscopic equation as presented in Equation 4.1.

$$\Delta\nu = \Pi \cdot \sigma \tag{4.1}$$

For both the thermally grown oxide and the ceramic top coat, the thickness values were idealized as thin films due to the geometry as showcased in Figure 4.4B.

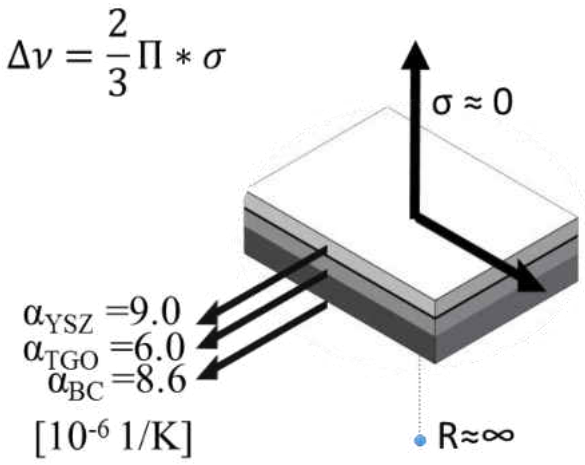

Figure 4.4: Biaxial Assumption for Thin Films and Thermal Expansion Mismatch [59]

This allowed the use of the biaxial assumption, and led to a modified Piezospectroscopic equation presented in Equation 4.2. It can also be seen that the thermal expansion mismatch is quite large, and this leads to large residual stresses after cool-down from high temperature. A piezospectroscopic coefficient of 7.59 cm^{-1}/GPa for R1 and 7.61 cm^{-1}/GPa for R2 respectively was used in conjunction with the zero stress reference peak center of 14403 cm^{-1} and 14433 cm^{-1}. [11, 63, 118]

$$\Delta\nu = (2/3) \cdot \Pi \cdot \sigma \tag{4.2}$$

The stress map by method of the R1 optical peak center is presented in Figure 4.5 using the biaxial stress assumption.

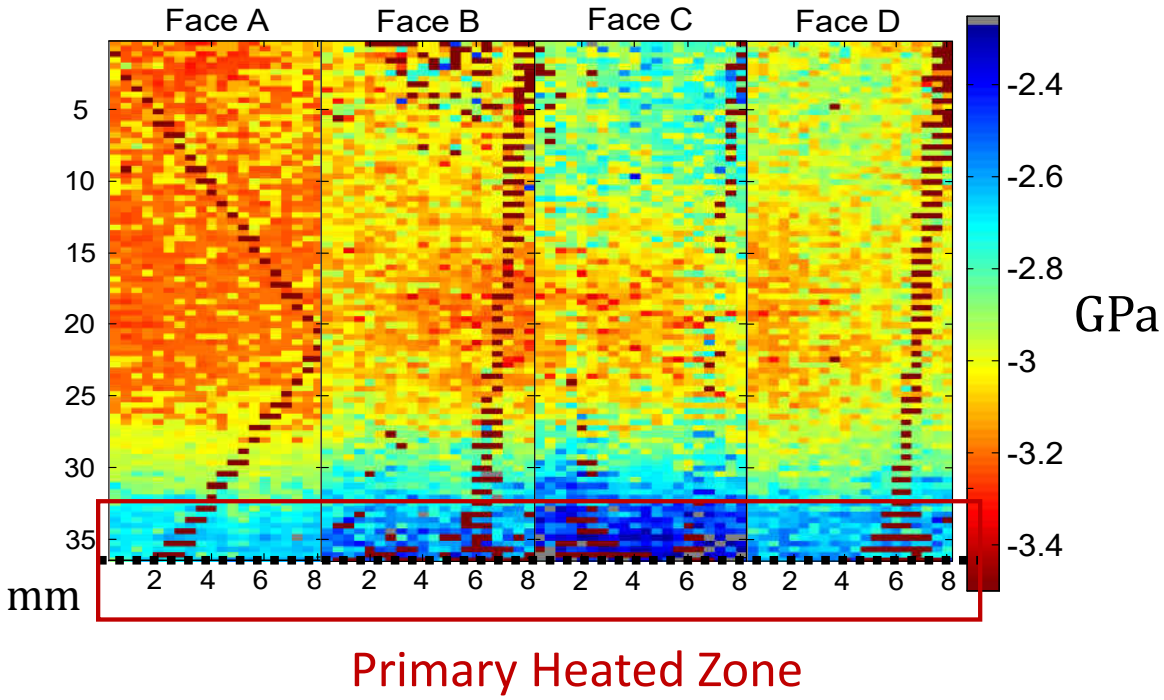

Figure 4.5: Stress Map of the Thermally Grown Oxide on an Early Aged Specimen by Photoluminescence via R1 Optical Peak

The loading conditions that drove the residual stresses are presented as well. Each scanned face, A, B, C, and D, are presented with a 2000 point stress contour map, with varying stress of approximately 3.25 GPa to 2.75 GPa. The primary heated zone center is located as well, and from the map a stark comparison can be identified. It can be

observed that the thermal drop due to heater focusing is influencing the stress value in the thermally grown oxide.

This is due to the mechanics of oxide growth, where during early aging the oxide grows very quickly [59, 131]. The stress values for the primary heated zone, which was held at 1000 °C, is substantially lower than rest of the map. This suggests that the initial growth of the oxide is reducing the stress observed by the Photoluminescence spectroscopy method under the biaxial assumption, which is not unexpected [129].

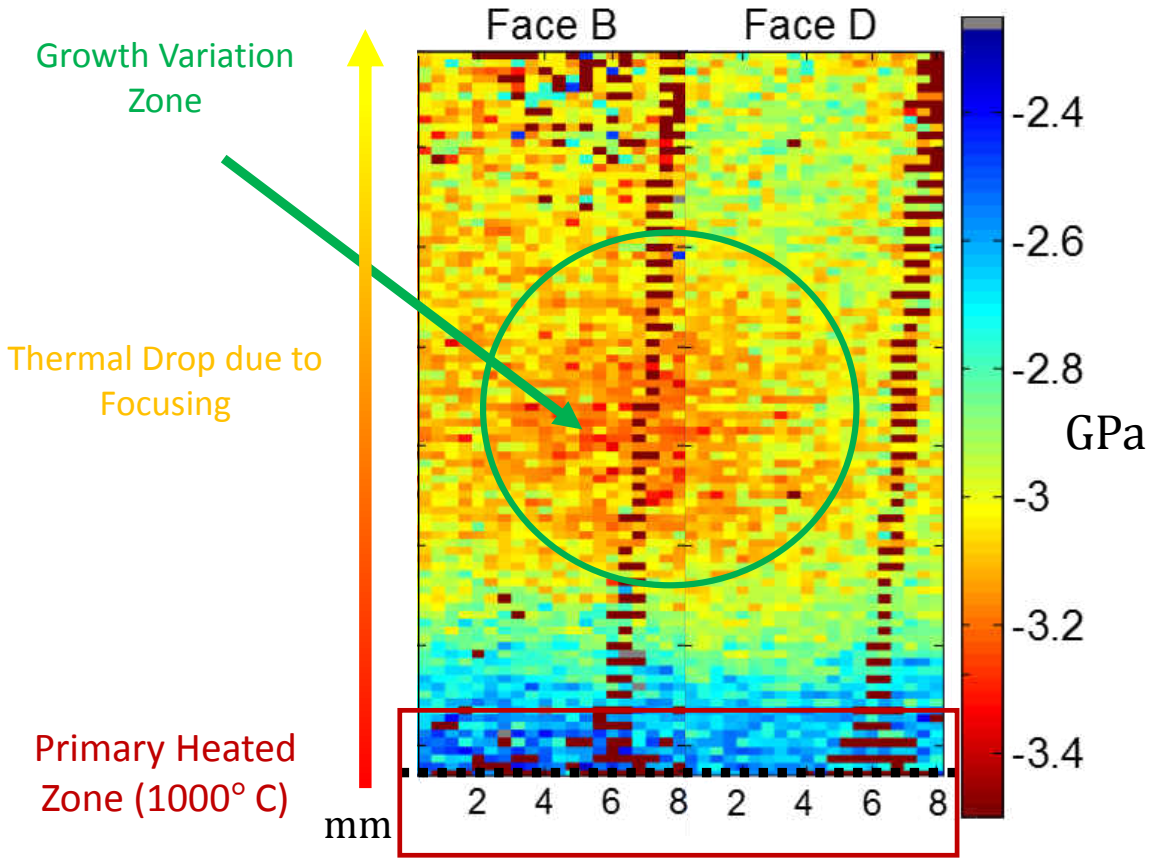

Figure 4.6: Linking Thermal Variations with TGO Stress

Figure 4.6 condenses the four face maps to just Face B and D. This can be done due to the 360° of overlap taken by the map. This was beneficial as Face A may have been impacted due to stray ambient light and a shutter timing mismatch. Face B and D provide a full map of the circumference of the specimen scanned area, with height of 40 mm. A growth variation zone is also detected in the middle of the scanned zone, marked

in the green circle. Here stress values are significantly higher, 250 MPa greater than the background zone, and 500 MPa greater than the primary heated zone.

Figure 4.7 presents the stress map for the early aged specimen via the R2 optical peak. This compliments the findings presented in Figure 4.5, and it can be observed that the stress values are in line with one another. Furthermore, the same trends are visible including the uniformity of the primary heated zone and the presence of the anomalous growth variation in the center of the map.

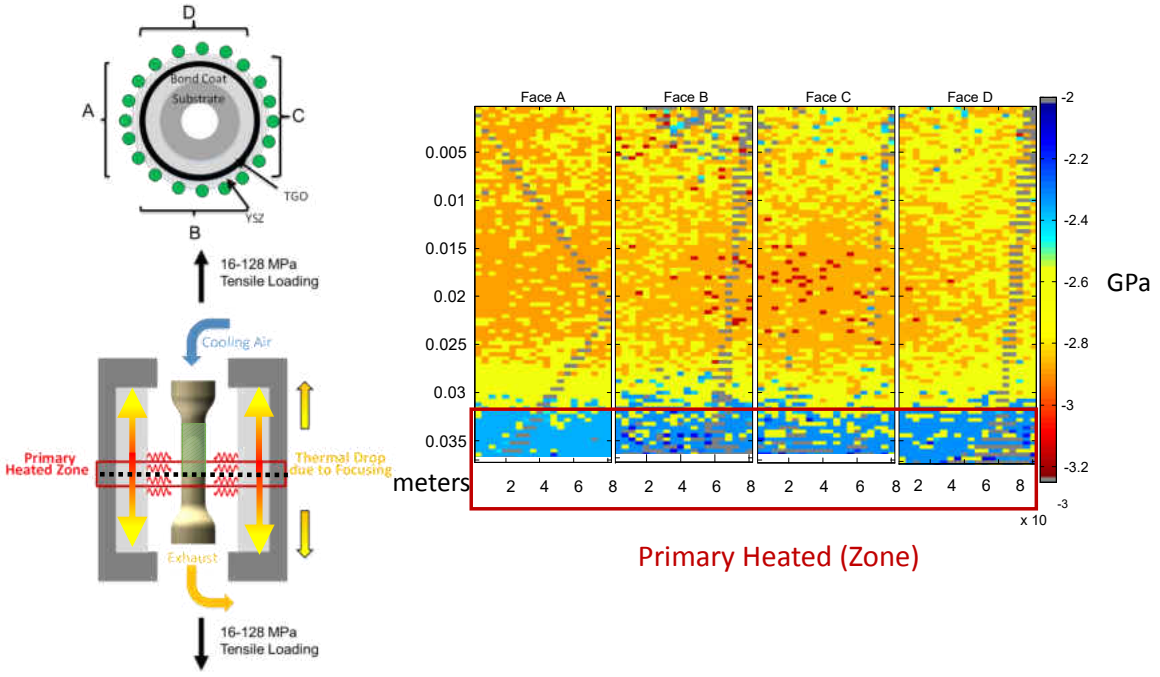

Figure 4.7: Stress Map of the Thermally Grown Oxide on an Early Aged Specimen by Photoluminescence via R2 Optical Peak

A comparison of the stress values as determined from both the R1 and R2 optical peaks is presented, showing approximately an 8% deviation in the calculated value. A map of the deviation corresponding to the full measurement scan is presented in Figure 4.8. The deviation was seen to be overall rather uniform. This investigation was done in part to identify if there were any local regions exhibiting a higher degree peak splitting, which is known to be a sign of damage. [53]

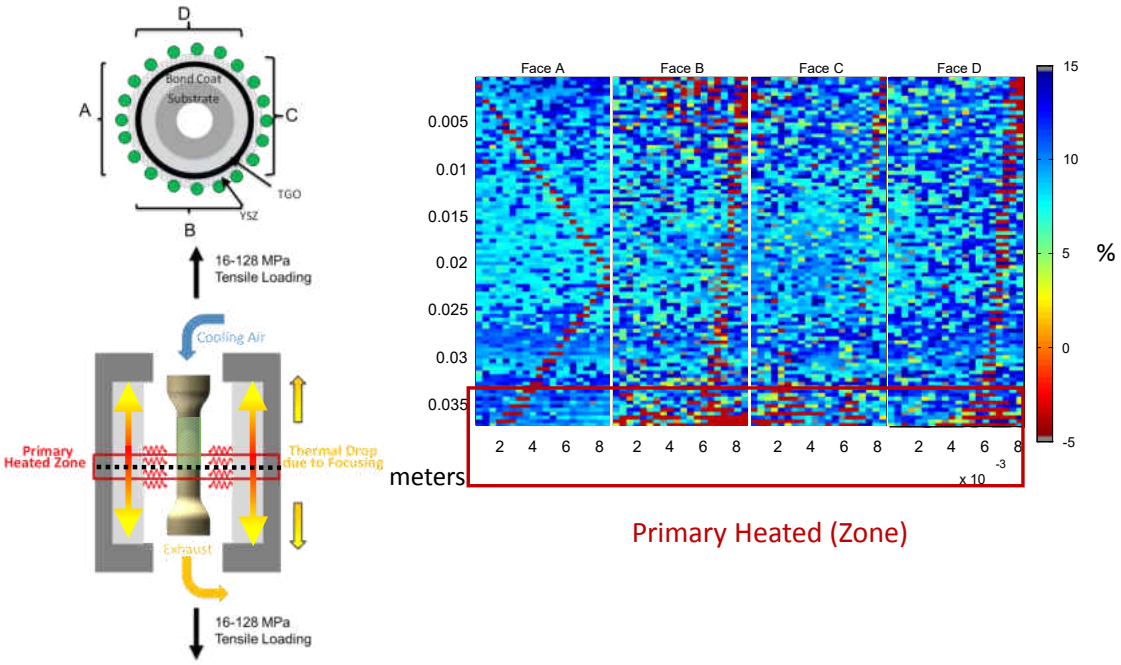

Figure 4.8: Map of the Thermally Grown Oxide Stress Deviation Percentage as Calculated via the R1 and R2 Optical Peaks

4.3 Raman Spectroscopy of Yttria-Stabilized Zirconia Top Coat From Early Cyclic Aging

Initial scans of the thermally grown oxide revealed the characteristic optical spectra of Yttria-stabilized Zirconia on the CCD. The finding is presented in Figure 4.9. Several peaks can be identified from the CCD with varying intensity. The intensity from the Raman effect is not as powerful as the α-alumina luminescence. It can be noted that the scan was completed in the absence of majority of ambient light to maximize the collected intensity.

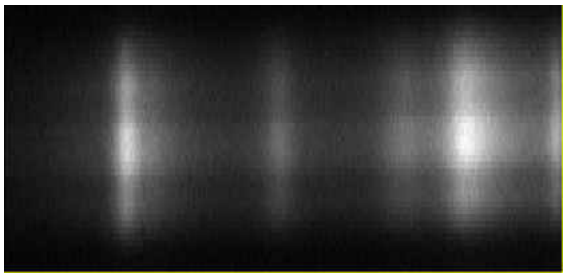

Figure 4.9: Collected Optical Spectra of Yttria-Stabilized Zirconia on CCD

The collected Raman spectra for Yttria-stabilized Zirconia has been plotted in Figure 4.10.

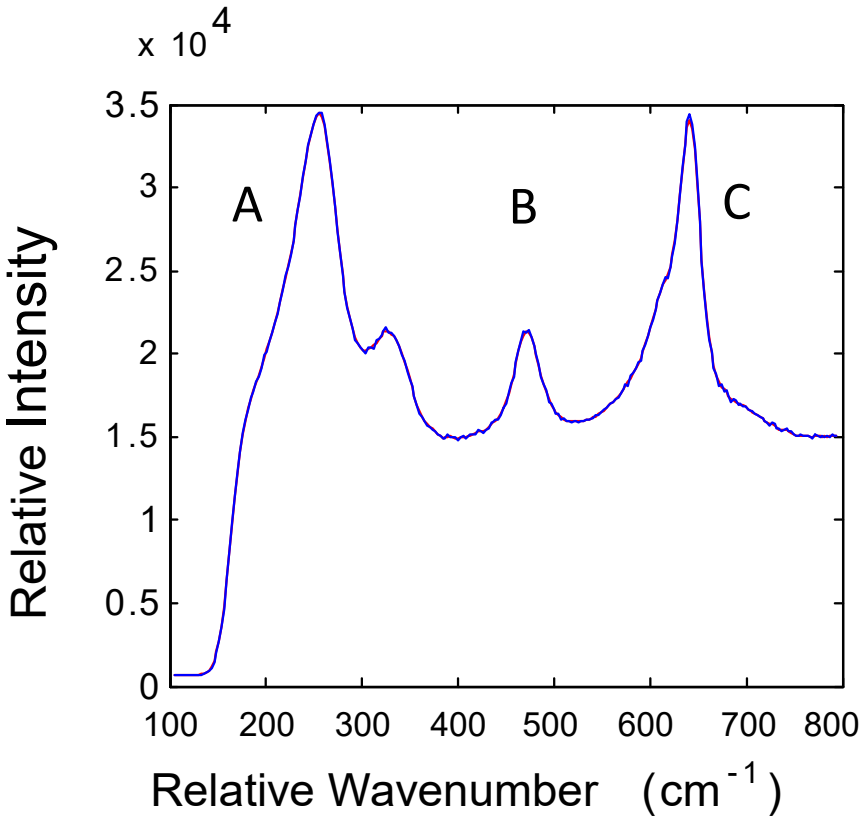

Figure 4.10: The Raman Spectra of Yttria-Stabilized Zirconia

A total of five peaks were identified, with three peaks being available for fitting. These spectra matched well with literature, with the selected peaks representing the 258 cm^{-1}, 463 cm^{-1}, and 638 cm^{-1} bands from literature [78, 50]. The approximate values collected in the map were 255 cm^{-1}, 470 cm^{-1}, 641 cm^{-1}. The fitting of these peaks is showcased in Figure 4.11.

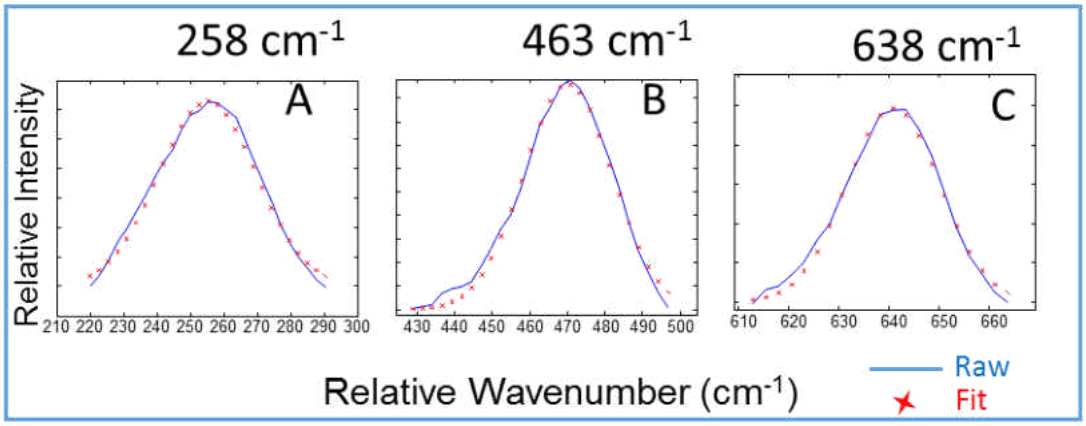

Figure 4.11: Peak Fitting for Yttria-Stabilized Zirconia

The collected spectra was compared with literature for phase identification. [21] Chambers et al. performed a study varying the percentage of phase composition for stabilized zirconia. This allowed a comparison with the spectra collected, of which it was observed to have only tetragonal prime zirconia. All other phases, including monoclinic and cubic, were ruled out.

These bands at 258cm^{-1} and at 638 cm^{-1} are expected to shift in opposite directions due to compressive stress [78]. This is likely due to softening of the mode due to hydrostatic stress of the 258cm^{-1}. [17] This peak at 258cm^{-1} corresponds to the E_g lattice

vibration. [84]. One peak found in literature was not evident in the collected scan presented in Figure 4.10. The location of the 145 cm^{-1} peak from literature was too close to the laser line for the Princeton Instrument's spectrometer. A Renishaw RM-1000 Ramascope with a 1800 groove/mm grating was employed by way of a microscope with a 10x Nikon objective. This proved to be effective, capturing a distinct peak at 144 cm^{-1}. This completed the literature comparison with all the reference peaks. The captured peaks from the Ramanscope is presented in Figure 4.12.

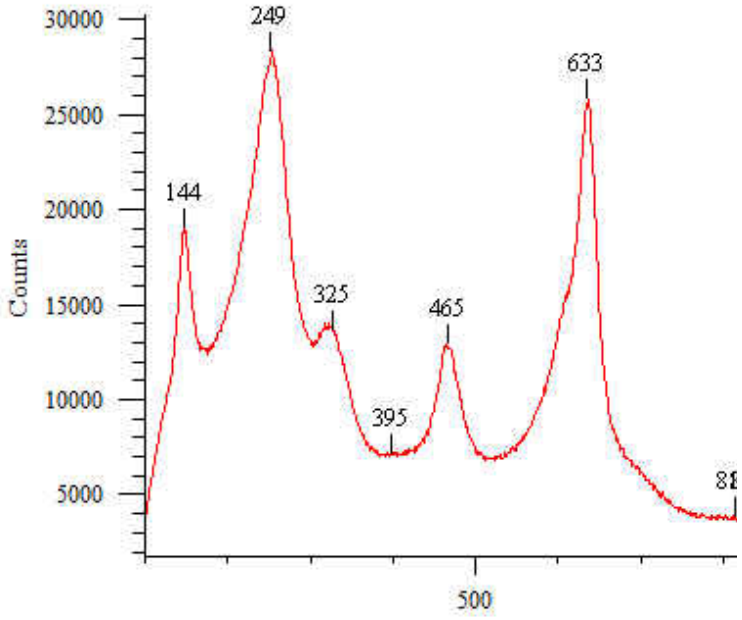

Figure 4.12: Collected Optical Spectra of Yttria-Stabilized Zirconia via Micro-Raman for Identification of Peak Close to Laser Line

For fitting, the 638 cm^{-1} peak has been traditionally used for accurate results due to its sensitivity to stress and excellent signal to noise ratio. [111, 126, 130, 78] For turbine coatings deposited by atmospheric plasma spray, this method is not advised as the less intense peak at 608 cm^{-1} is more prominent. [81] Herein, plots of the 258 cm^{-1} and 638 cm^{-1} peaks will be presented, as the sample was mapped circumferentially using Raman spectroscopy.

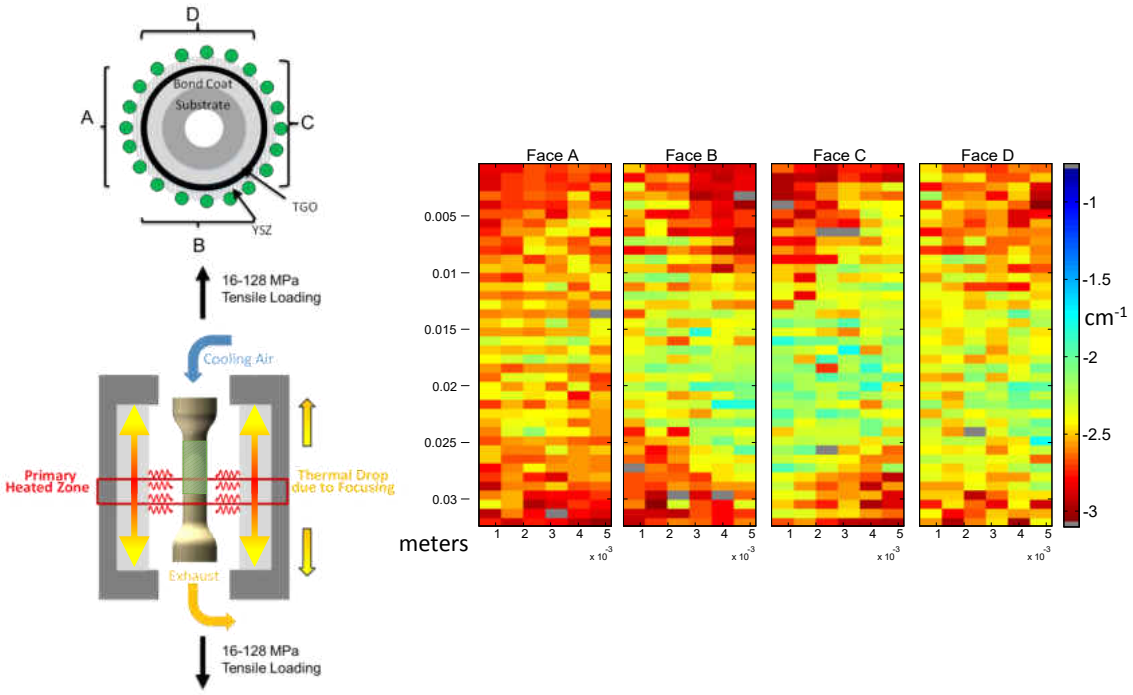

Figure 4.13: Raman Peak Shift Map from Zero Reference of 258 cm^{-1}

The results herein present the peak shift contour maps for the Raman study of the zirconia top coat. Stress values were not able to be calculated, however, due to the role of

heat treatment in influencing both the zero stress reference peak center and the piezospectroscopic coefficient. [87, 79] Because the collected spectra only varies approximately 3 cm^{-1} to 5 cm^{-1}, the selection of a zero reference center would cause the calculated stress value to near double due to variation in the reported references. [84, 87, 79, 81] Here the presented peak shift is representative of the variations in the stress value, and as such can be utilized in the study.

Figure 4.13 presents the contour map of the variation in peak center from the 258 cm^{-1} reference peak. It can be seen that the zone below .03 meters of the y axis, corresponding with the primary heated zone, appears to have a uniform peak shift from stress free reference of approximately -3 cm^{-1}. A region of interest presents itself in the center of the map, matching the area of higher stress found in the thermally grown oxide stress map. The presence of both of these features suggests that the development of the thermally grown oxide has a marked effect on the stress profile of the zirconia top coat.

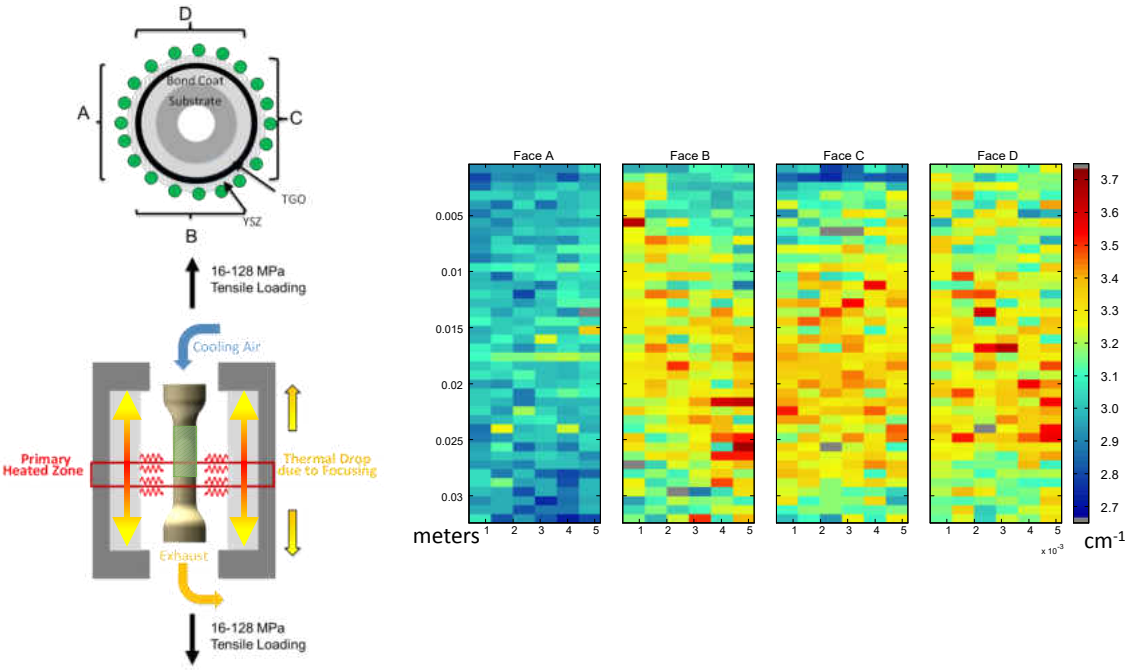

Figure 4.14: Raman Peak Shift Map from Zero Reference of 638 cm^{-1}

Figure 4.14 presents the contour map of the variation in peak center from the 638 cm^{-1} reference peak. Congruent with the 258 cm^{-1} peak's results, the primary heated zone appears to have a uniform peak shift from reference at approximately +3 cm^{-1}. A similar region of interest presents itself in the center of the map, matching the area of higher stress found in the thermally grown oxide stress map and the 258 cm^{-1} peak's results. The presence of both of these features in both peak's maps suggests that the development of the thermally grown oxide has a marked effect on the stress profile of the zirconia top coat.

4.4 Comparison of Early Cycling vs. Aged Specimen

The specimen was aged in a furnace at the German Aerospace for 264 additional hours at high temperature. The role of long duration aging on the stress state and damage mechanisms of the thermally grown oxide and ceramic top coat is the focus of this investigation.

4.4.1 Photoluminescence of Thermally Grown Oxide Following Long Duration Aging

The stress map by method of the R1 optical peak center, after the aging process, is presented in Figure 4.15 using the biaxial stress assumption. The loading conditions that drove the residual stress are presented as well. Thermal loads applied are not influenced by heater focus inciting a thermal drop, nor the effect of cooling gradients. It was hypothesized that the variations of the stress profile would fade away due to long duration uniform heating.

Each scanned face, A, B, C, and D, are presented with a 2000 point stress contour map, with varying stress of approximately 2.75 GPa to 3 GPa. From the map it is evident that the degree of uniformity has increased due to long duration isothermal heating. There are unique features which deviate the uniform stress field, likely due to subtle variations in the furnace.

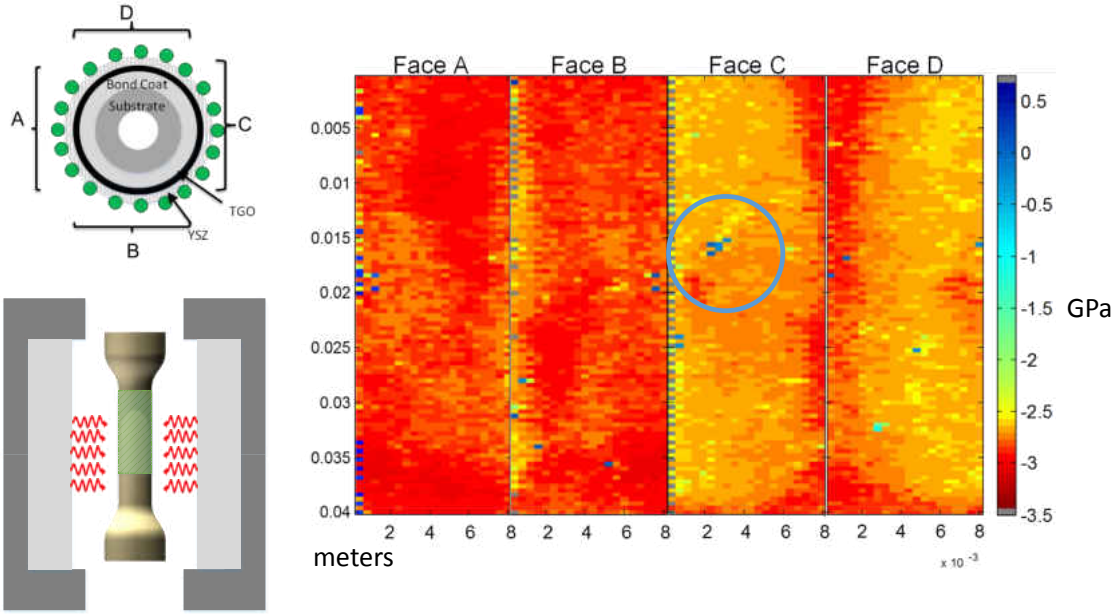

Figure 4.15: TGO Stress Map (R1) of an Aged Specimen with Identified Microdamage

Variations in the map would be driven by the mechanics of the oxide growth. The growth mechanism slows as diffusion is limited due to the increase in oxide scale thickness. Thermal loading was near uniform at 1000 °C. The stress values were determined by the modified piezospectroscopic equation, with the biaxial assumption. Comparing with the early cyclic aged stress map in Figure 4.5, it can be observed that the stress state of the sample continued to decline slightly from the highest regions representing minimum TGO growth. As the loading conditions were nearly uniform, the previous effects of thermal gradients appear to be removed. However, under service conditions non-uniform loading

due to aerodynamic influences and forces may in fact have a long duration effect on the stress state development and the material's response.

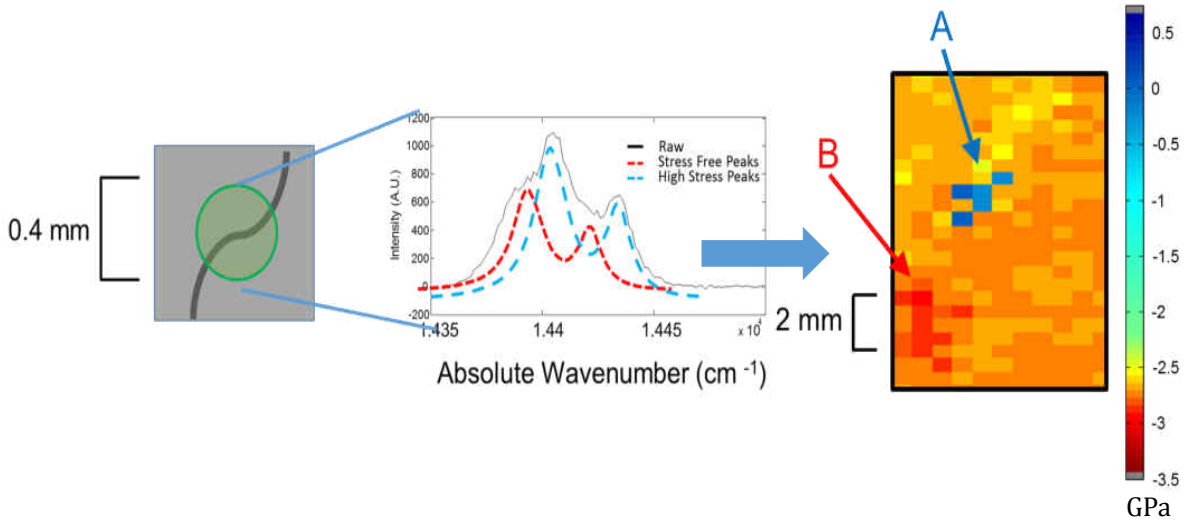

Figure 4.16: Dual Stress States Presented in Scan Over Micodamaged Zone with 3GPa Variation

Highlighted is also a region where micro-damage has occurred in the oxide. A dual stress state is suggested by the broadening and presence of smaller secondary characteristic optical peaks for α-alumina. Presented in Figure 4.16, the effect is understood to be caused by micro-damage with a size falling inside the laser scanning diameter, yielding a dual stress state of both 3 GPa and 0 GPa for the measurement location.

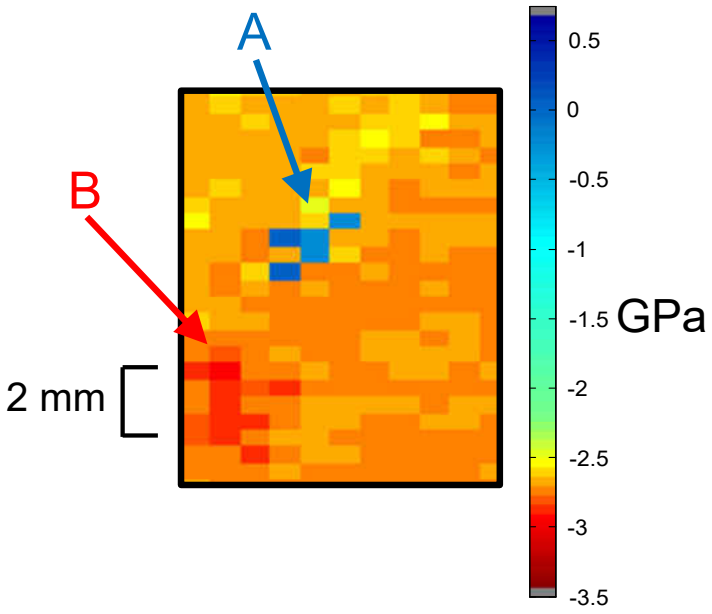

Figure 4.17: Observed Micro Damage

The possible micro-damage is focused on in Figure 4.17 marked in A. A region of higher stress can be identified on one side of the stress free zone, accompanied by a reduction in stress on the other front from the local average. Close by, a pocket of considerably higher stress is observed marked in B. The nondestructive technique has shed light on the mechanisms of damage in the specimen due to aging. This image provides a look into the mechanics of thermally grown oxide micro spallation, whereby a small segment of approximately 500 μm appears to be lifted. This micro damage is seen to have an impact on the coating directly around the damaged zone.

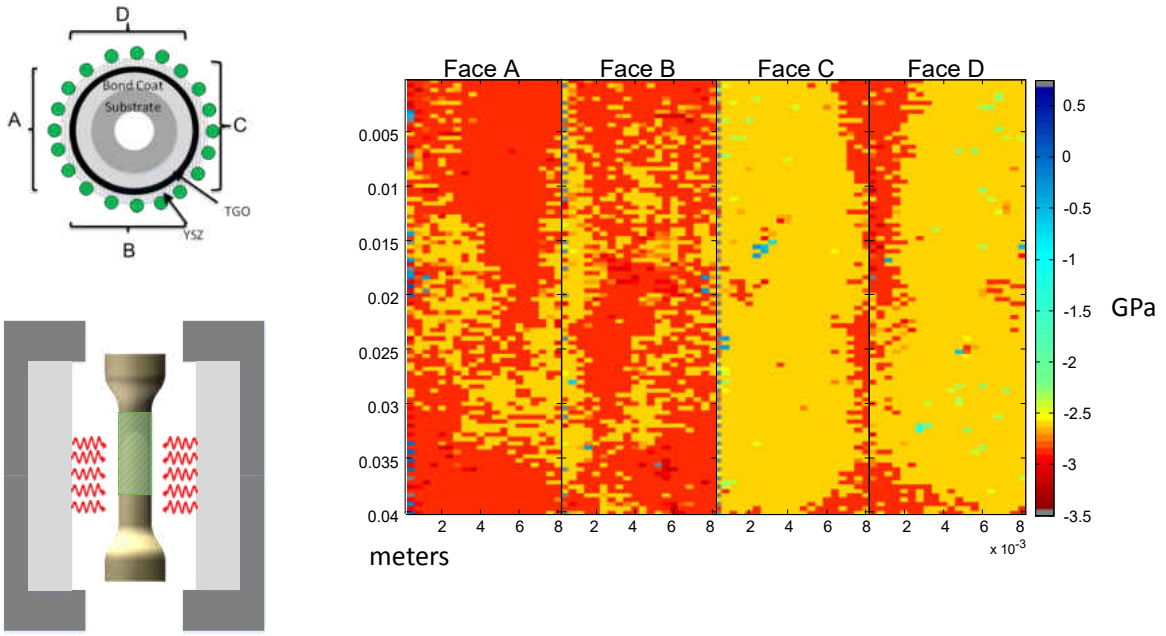

Figure 4.18: Stress Map of Aged Oxide via R2 Optical Peak

The stress map using the R2 optical peak was also presented in Figure 4.18 for comparison. The profile has a similar distribution as with the R1 stress map. Micro damage is again observed in the R2 peak with a similar stress profile.

For comparison the deviation between the R1 and R2 stress map values was presented in Figure 4.19. The profile was observed to be quite uniform with variations of approximately 150 MPa.

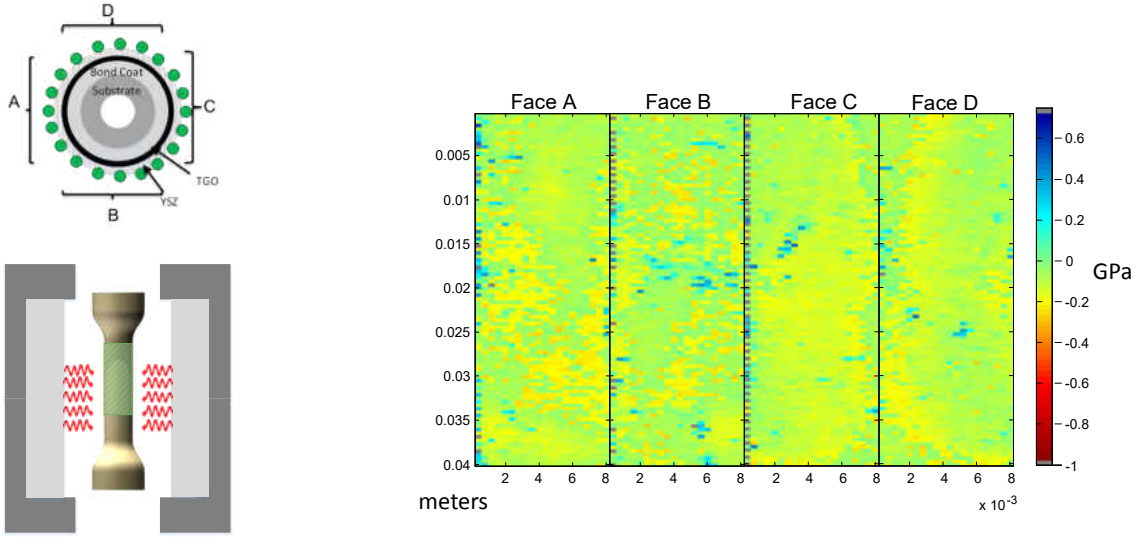

Figure 4.19: Difference of the Resulting Stress Values from R1 and R2 Peaks of α-Alumina via Photoluminescence

4.4.2 Raman Spectroscopy of Yttria-Stabilized Zirconia Top Coat Following Long Duration Aging

Stress maps for the zirconia ceramic top coat for peaks 258 cm^{-1} and 638 cm^{-1} were generated and presented in Figure 4.20 and Figure 4.21. The outer most column of data was removed due to edge effects from the scanning method, where the laser scanned to the edge or off the specimen. Both maps are nearly uniform with variations of 0.1 cm^{-1} to 0.4 cm^{-1}. This small deviation is approaching the limitations of the spectrometer and

the fitting certainty, and could be considered in large part uniform. This is expected from the long duration aging of the specimen.

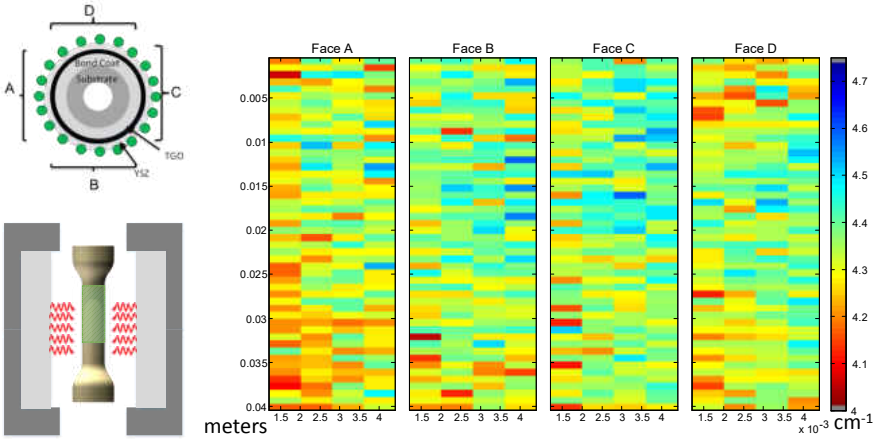

Figure 4.20: Peak Location Map for Aged Zirconia (Peak 258 cm^{-1})

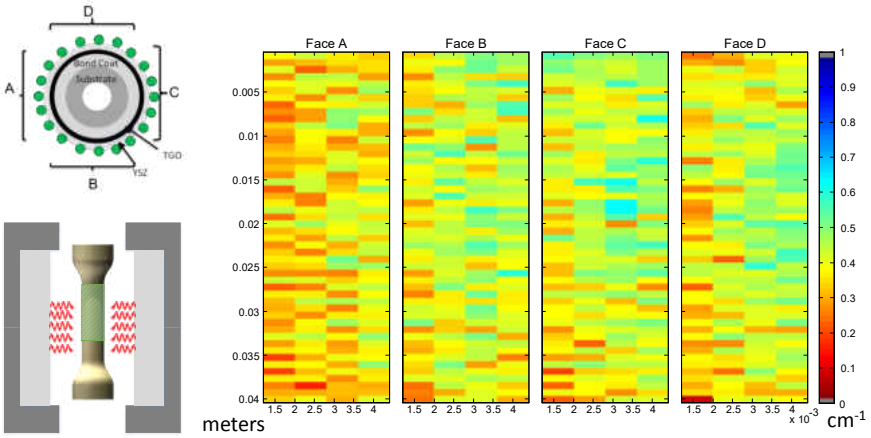

The change observed from the early cycled map to the long duration aged map of the peak shift for the YSZ was plotted in Figure 4.22 and Figure 4.23. Here it is to be noted that the scan conducted on the aged specimen was lengthened to match the 40 mm height covered by the luminescent scan. As such, the area in which the early aged specimen was not scanned is presented in gray.

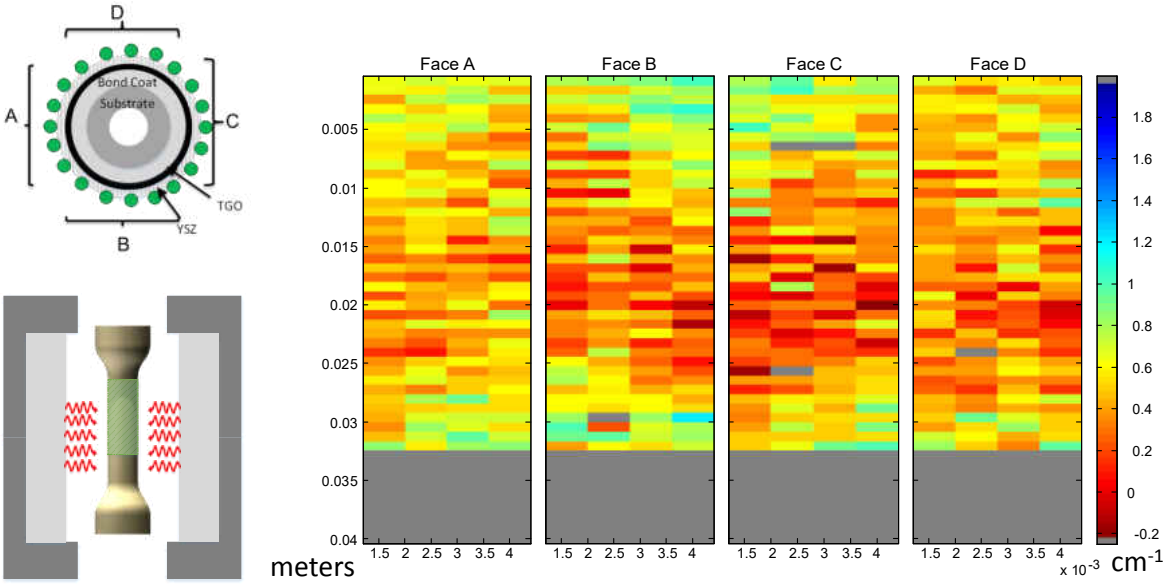

Figure 4.22: Map of the Shift in Peak Center from Early Cycled to Long Duration (Peak at 258 cm^{-1})

In both maps it is evident that greatest change lies in the zones that were less dramatically shifted in the pre-aging due to thermal drop and induced cooling. This showcases that the zones that had experienced less intense aging were brought to be uniform with

the rest of the specimen, suggesting that the long duration at near uniform high temperature has undone the variation in development from the complex and deviating loading conditions. This also suggests that if left in non-uniform thermal conditions during aging, effects may remain on the sample having a marked effect on the residual stress state in the coating layers.

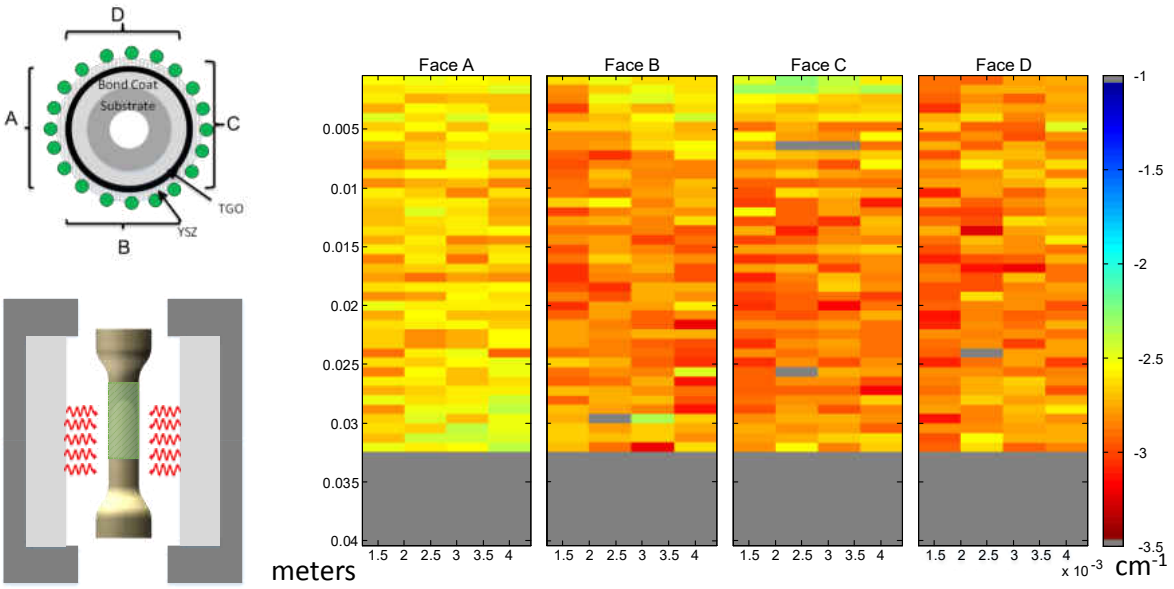

Figure 4.23: Map of the Shift in Peak Center from Early Cycled to Long Duration (Peak at 638 cm^{-1})

4.5 Conclusions

In this chapter several significant conclusions can be taken from the experiments and results. Nondestructive testing techniques were able to perform phase and constituent identification and shed light on the response to loading conditions. It was found that the development of the thermally grown oxide, under varying thermal loads, is non-uniform and subject to high stress gradients over small distances. Stress maps showcase a sharp 0.5 GPa stress variation over a few millimeter region. Further, the variations in the oxide layer's stress profile was seen to have marked effects on the ceramic top coat's stress distribution.

Raman spectroscopy probed the ceramic top coat and allowed for phase identification of the Yttria-stabilized Zirconia. The variation of the stress field was observed through the deviation in peak center following peak fitting. The stress profile was seen to follow the trends found through the Photoluminescence spectroscopy of the oxide scale, suggesting the oxide development has a marked influence of the ceramic top coat.

Aging of the specimen for long duration at near uniform thermal loading was shown to unify the stress profile for both the thermally grown oxide and the zirconia top coat. The aged oxide presented a decrease in stress, calculated under the biaxial assumption, due to growth and development with its highest stress value being during early stages of growth.

Micro damage was observed in the thermally grown oxide, suggesting the onset of damage from the aging process. These zones were seen to have an effect on the attached coating around them, as complex stress gradients were observed. The findings also suggest that long duration aging under dynamic and varying loading conditions may establish stress profile variations that lead to changes in material response, damage propagation, and failure mechanics.

CHAPTER 5
X-RAY DIFFRACTION FOR STRAIN ANALYSIS OF THERMAL BARRIER COATING SYSTEMS

Synchrotron X-Ray Diffraction is an effective nondestructive testing approach that in conjunction with piezospectroscopy can provide a more complete investigation of a multi-layer coating system.High energy X-Rays afford the throughput to measure the as-coated specimen's strain in each of the thermal barrier coating system's layers.

5.1 Objectives

The objectives of the X-Ray Diffraction experiments included identification of the coating's constituents and phases, as understanding variations in a material's phases due to thermal loads and cycling, sheds light on the stability of the coating. The loading conditions' representative of the effect of service conditions of a turbine on the strain profile during ambient conditions, ramp-up, and high temperature holds were investigated. Results from this method in conjunction with the piezospectroscopic measurements are to be used to more completely understand the material response, damage mechanisms, and influence of loading conditions over the lifetime of the samples.

5.2 Discussion of Results

The setup and measurement location for the as-coated specimen is presented in Figure 5.1. The measurement was conducted utilizing the grazing method as shown in Figure 2.4. The scan averages the measurement through the material it passes through en-route to the detector. Small effects from double diffraction due to the change in material composition resulting from the cylindrical specimen were expected and observed, with minimal peak broadening. The measurement zone was located in the center of the gauge section, appropriately in the region assumed to be uniform in thermal loading. This expectation was validated following the synchrotron measurement by utilizing piezospectroscopy as seen in Figure 4.6.

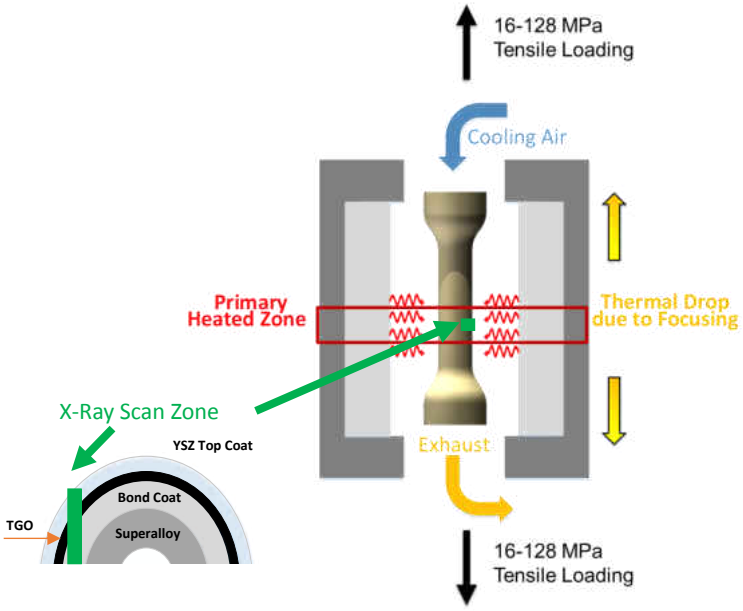

Figure 5.1: X-Ray Diffraction Scanning Location and Applied Loading Conditions

The thermal cycle investigated was that of a representative flight cycle: ramping up from the ambient condition for 20 minutes, a high temperature hold at 1000 °C for 40 minutes, and concluding with thermal ramp down for 20 minutes. The conditions are presented in Figure 5.2, which shows the loading conditions during the experiment.

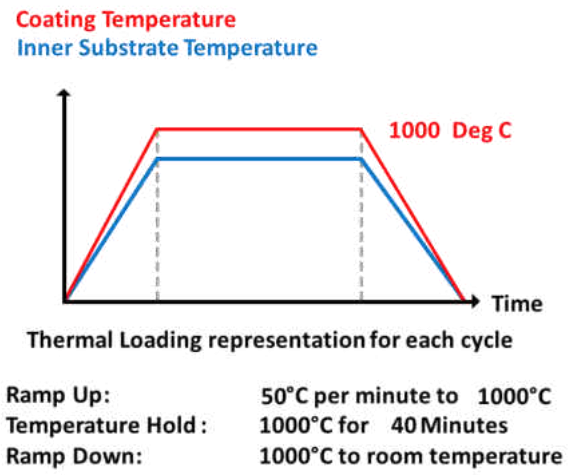

Figure 5.2: Representative Flight Cycle for in-situ Measurements

Each cycle scan was conducted with 5 frames per measurement location, with 10 measurement locations over the sample thickness. The step size was 30μm per discrete measurement location. A schematic detailing the locations are is presented in Figure 5.3 This scanning methodology is further explained in Chapter 3. Due to the geometry, the resulting diffraction rings had multiple layers present. Strain analysis techniques are able

to determine strain profiles for multiple phases and crystallographic planes that appear on the same ring pattern without concern of interaction.

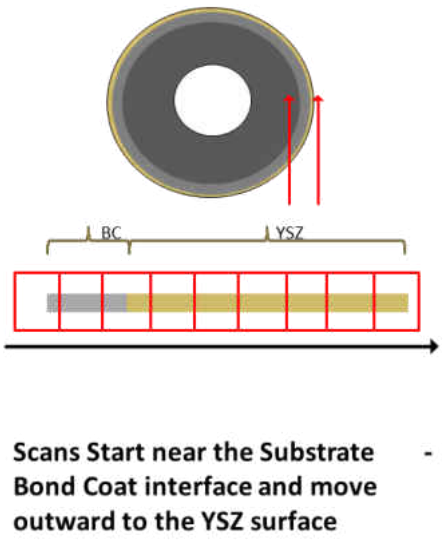

Figure 5.3: Scanning Locations Across the Coating System

5.2.1 Phase Identification

The collected Debye-Scherrer diffraction rings for the Thermal Barrier Coating system are presented in Figure 5.4. Several phases and constituents are identified in the MCrAlY bond coat and the zirconia topcoat. Tetragonal prime Yttria-stabilized Zirconia was identified in the top coat. This was confirmed with the piezospectroscopy study presented

in Figure 4.10. Raman spectroscopy also allows for identification of tetragonal double prime, whereas X-Ray diffraction cannot observe changes due to oxygen vacancies. [137, 84, 138]

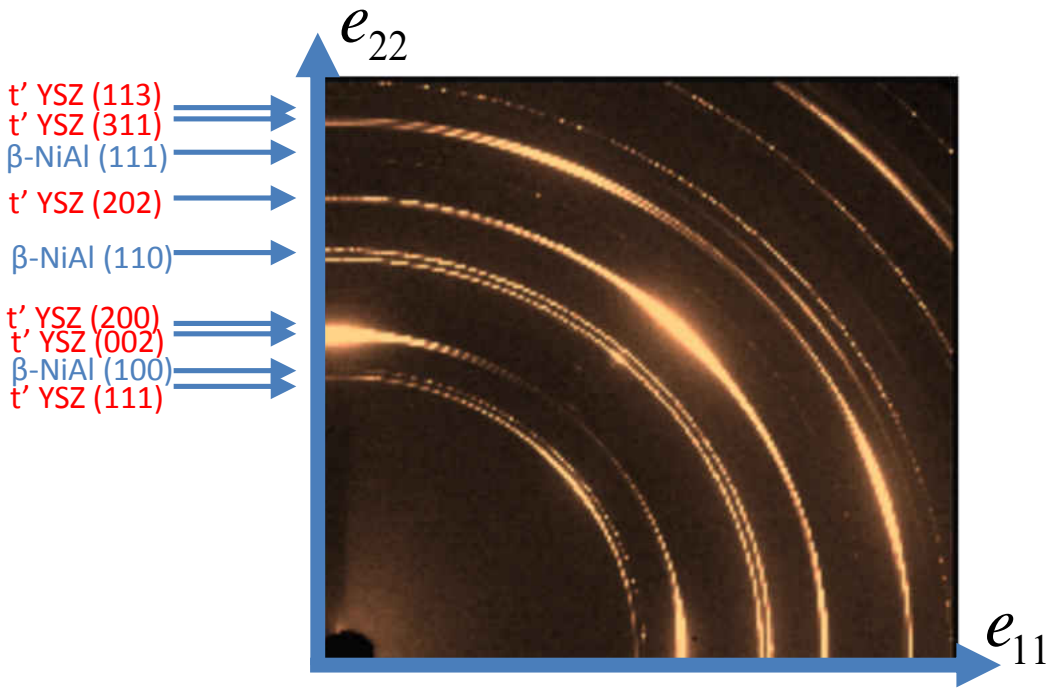

Figure 5.4: Phase Identification Conducted for a TBC Specimen [71]

To determine the zero strain reference for diffraction measurements, two methods can be conducted. Powder diffraction can be conducted, where the powder form of the material is the reference zero strain. [56] However, this method can be challenging depending on the material or composite. When investigating high temperature phase changes, it becomes difficult to determine a zero reference. A second method that is

feasible is measuring the invariant strain crossing angle, denoted by η^*. [2] This is of great use to the study as the crossing point is also invariant to temperature. In this study, the laboratory coordinates align with the principal strain axis. However, with varying loading conditions, shear strain caused the ellipsoidal axis to rotate and further analysis has to be done to resolve the principal axis.

A Matlab routine specific to the loading conditions in the experiment was developed in-house to determine the crossing angles for use in strain analysis. In Figure 5.5, a representation of this method is presented. The parameter η^* is determined as an angle around the azimuth, and is used as the zero strain reference angle.

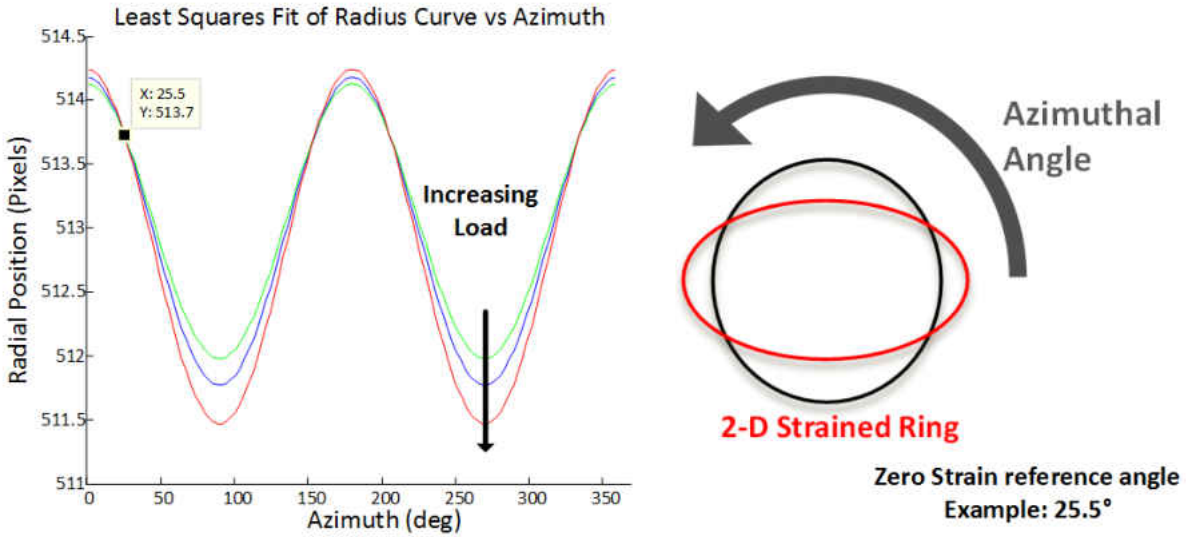

Figure 5.5: Strain Invariant Angle Determination for Strain Analysis

The averaged intensity value around the azimuth is presented in the form of intensity vs. d-spacing plot in Figure 5.6, where d-spacing represents the inter-atomic spacing in the crystal in Angstroms. Here visible undulations are present, a marked sign that thermal expansion is affecting the material crystallographic plane of the constituent or phase. Variations in phase composition can be noted where additional peaks will rise in intensity due to thermal loading.

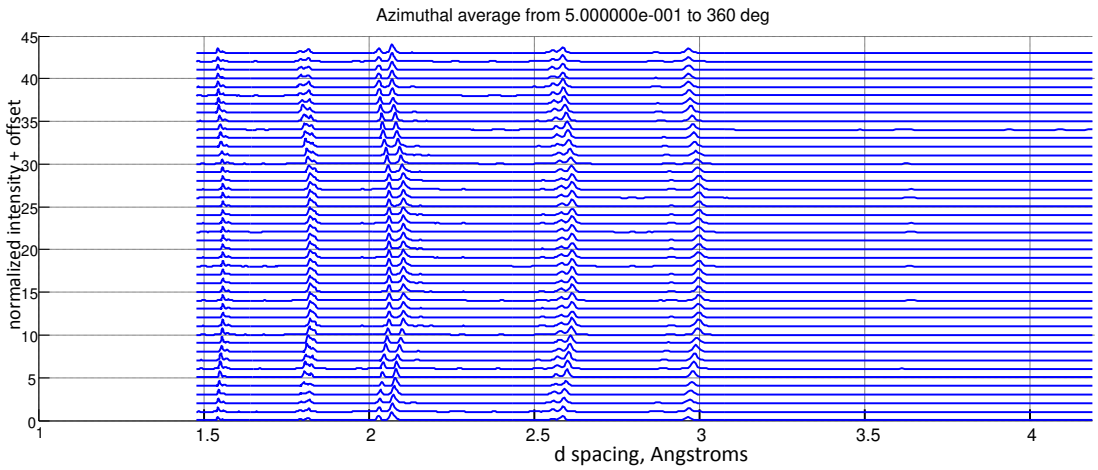

Figure 5.6: Intensity vs. D-Spacing Plot Through Thermal Cycle with Visible Undulations Due to Thermal Expansion in Response to Thermal Loading

5.2.2 Strain Profiles of MCrAlY Bond Coat

The full cycle plot of strain for the MCrAlY bond coat is presented in Figure 5.7. Two phases of the bond coat are presented, β-NiAl and γ Ni solid solution. The e_{11} and e_{22} strains are plotted for β-NiAl 100, β-NiAl 110, and γ Ni solid solution 111. The 80 minute scan was conducted under 64 MPa of mechanical loading, a surface temperature held at 1000 °C, and with induced thermal cooling on the internal substrate wall with 75% of the maximum 100 SLPM flow rate.

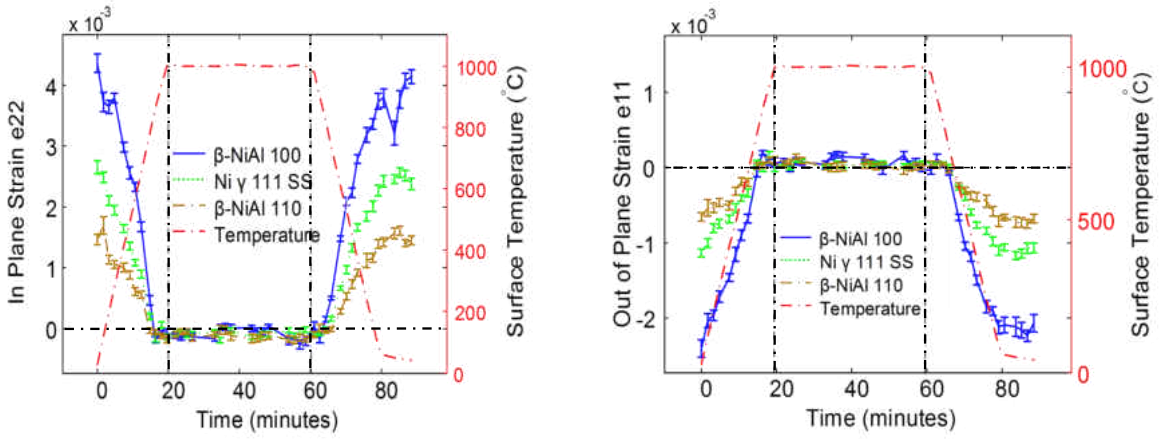

Figure 5.7: In-Situ Strain Profile for MCrAlY Bond Coat in Response to Representative Flight Cycle [70]

The effect on the strain due to the thermal load is clearly evident. At room temperature the e_{22} direction experiences tensile strain on the order of $2{\cdot}[10^{-3}]$ to $6{\cdot}[10^{-3}]$, while the e_{11} direction experiences compressive strain on the order of $-3{\cdot}[10^{-3}]$ to $-14{\cdot}[10^{-3}]$.

Anisotropy is visible in the variation of strain between the planes, which is variable with temperature. Strain relief is observed at high temperatures in the e_{11} and e_{22} profiles, with the strain response for e_{22} turning slightly compressive and the e_{11} becoming slightly tensile. The strains return to their higher state during ramp down. Another finding of interest is that the bond coat strain converges to its high temperature strain relief value before the thermal cycle has time to reach the hold temperature of 1000 °C, which would suggests a non-linear behavior response. This is an important finding for advancing numerical modeling, and will be investigated further in the future work.

5.2.3 Strain Profiles of Yttria-Stabilized Zirconia Top Coat

The full cycle plot of strain for the Yttria-stabilized Zirconia top coat is presented in Figure 5.8. One plane is presented, t'-YSZ 111, for the zirconia and the β-NiAl 100. These peaks were fit as a doublet due to their proximity. The e_{11} and e_{22} strains are plotted for the full 80 minute scan. Loading conditions were held at 64 MPa of mechanical loading, external surface temperature held at 1000 °C, and an induced thermal cooling on the inner substrate wall of 75% of the maximum 100 SLPM flow rate.

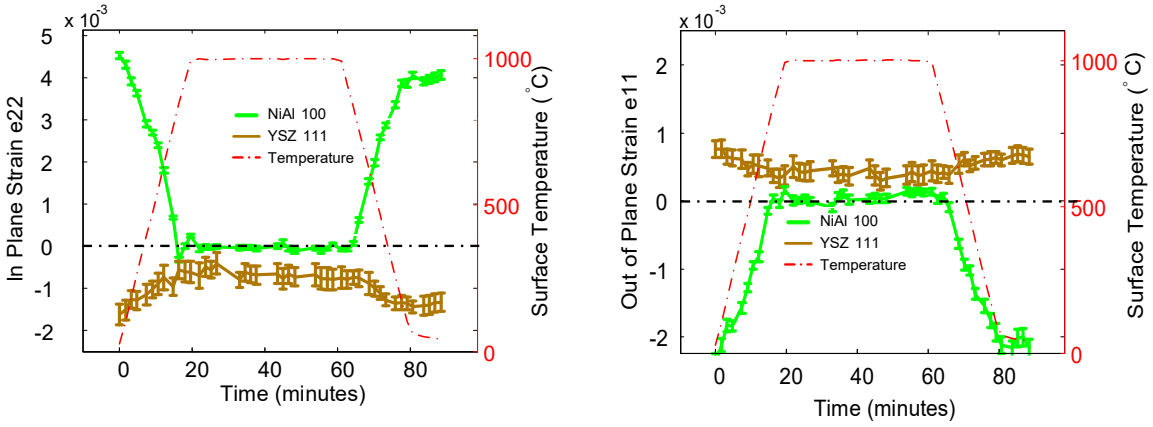

Figure 5.8: Strain Profile for YSZ in Response to a Representative Flight Cycle [70]

The effect on the strain due to the thermal load is clearly evident for the YSZ. At room temperature the e_{22} direction experiences compressive strain on the order of -2·[10^{-3}] while the e_{11} direction experiences tensile strain on the order of 0.75·[10^{-3}]. At high temperature strain relief is observed for both the e_{11} and e_{22} planes, with the strain response for e_{22} remaining slightly compressive and the e_{11} remaining slightly tensile. The strains return to their higher strain state during ramp down.

5.3 Conclusions

The X-Ray diffraction measurements afforded an investigation into the strain response of both the bond coat and top coat of the thermal barrier coating system. The thermally grown oxide was unable to be used for strain measurements in the as-coated condition,

as the diffraction volume was insufficient to stand out above a neighboring peak from the bond coat. This will be a study in the future work to conclude the cycle of testing with X-Ray diffraction studies on the long duration aged specimen.

From the piezospectroscopic studies conducted, the scanning location methodology for the diffraction measurements was validated as it identified that the region was uniform in the oxide scale development. Effects due to thermal loading during the representative loading cycle are distinct. At ambient temperature, both the bond coat and top coat phases showcase a high residual strain due to the thermal expansion mismatch from the coating temperature to the ambient. Upon returning to high temperature the strain state is reduced, and actually changes state from compressive to tensile or tensile to compressive. Anisotropic effects are also observed by measuring the strain in multiple crystallographic planes. Variation in the strain due to temperature was not observed to be equivalent between different phases in the bond coat, showcasing changes in anisotropy.

These results are beneficial to advancing material response models as high resolution, in-situ data was collected on a rapid time scale for thermal gradient and mechanical loading on a complex tubular geometry.

CHAPTER 6
PIEZOSPECTROSCOPIC STUDY OF KEVLAR® BALLISTIC PANELS

The nondestructive techniques techniques utilized for thermal barrier coatings can be applied for a variety of other aerospace materials. Of particular interest is that of fiber composites, which have application in ballistic armor and under high impact loading. The results herein will be presented for the piezospectroscopic study of Kevlar® ballistic panels following ballistic impact.

6.1 Objectives

The primary objective for this study was to map the region of a ballistic impact post ballistic testing. A scan of 25 mm by 25 mm was set to map the residual stress around the impact zone as seen in Figure 6.1. This allows for a more complete understanding of how impact and damage propagate through the fiber weave composite. The effects of different classes of nano-particle additives in the matrix of the composite will be investigated to understand how these features change the material response.

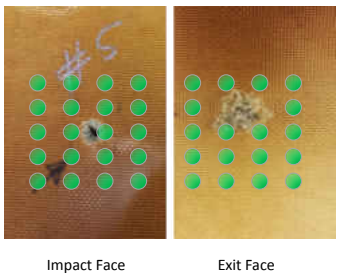

Figure 6.1: Scanning Objectives of Ballistic Damage on Kevlar® Composite Panel

6.2 Discussion of Results

The first consideration for examining Kevlar® 29 by Raman Spectroscopy was to capture the optical spectra from the pristine fibers, without matrix and additive effects, and to compare them with literature. The collected optical spectra from the pristine fiber is presented in Figure 6.2. This was compared with literature values found in Figure 3.3 [20, 69, 101, 134].

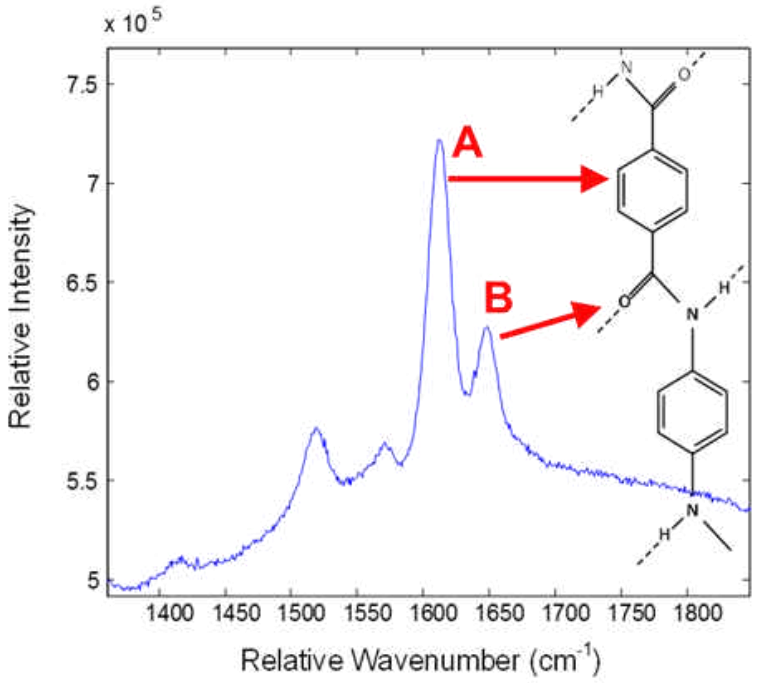

Figure 6.2: Pristine Kevlar® Fiber's Optical Spectra and Identification of Molecular Structure

A Renishaw RM-1000 Ramascope with a 1800 groove/mm grating was employed by way of a microscope with a 10x Nikon objective was utilized for measurements of the pristine fibers. The pristine Raman peak centers and standard deviation for the reference peaks at 1611 cm^{-1} and 1649 cm^{-1} are tabulated in Table 6.1.

Table 6.1: Tabulated Raman Readings for Pristine Fibers

	Pristine Fiber
Peak A Center [cm^{-1}]	1610.942
Standard Deviation of Peak A	.098
Peak B Center [cm^{-1}]	1648.512
Standard Deviation of Peak B	.300

From literature [134], it was able to be determined the molecular chain that incites the Raman response for each peak. The peak present at 1611 cm^{-1} results from the stretching of the C-C phenyl ring, while the peak centered at 1649 cm^{-1} results from primarily the C==O with a small percentage from the N-H [38]. The C==O and N-H bonds are held together loosely by the hydrogen bond and intermolecular forces [43], whereas the phenol ring stretches due to axial loads on the fiber chain. This knowledge of the molecular structure, coupled with the optical readings, allows for an in-depth examination of the load transfer throughout the fiber and the composite.

6.3 Additive Effects of Load Transfer

The effects of load transfer on the Kevlar® fiber was investigated using Raman spectroscopy. In Figure 6.3 the loading condition on a single fiber is idealized, and the molecular chains inciting the Raman response are marked. As the fibers are spun during manufacturing, they develop into long fiber chains. From the stretching of the phenol ring, the axial stress of fiber can be examined using the spectroscopic techniques. The weak bonding by the intermolecular forces that incite the secondary band at 1649 cm^{-1} represent the connection between each primary axially aligned fiber. The Raman response is comprised of the stretching of both bonds on each side of the connection. Here we can infer the intermolecular tearing stress on a single Kevlar® molecular sheet. These sheets are built up radially, until the entire packet forms a cylindrical fiber. Thus the measured Raman response has shed light on the internal radial stress of the fiber.

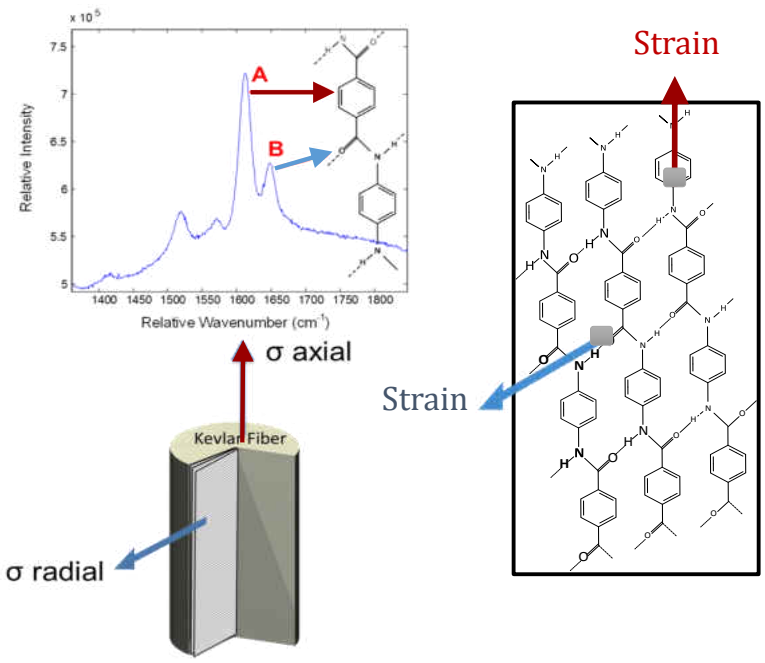

Figure 6.3: Linking the Molecular Structure and Piezospectroscopic Measurements to Load Transfer Throughout the Composite

The Baseline panel was scanned using the methodology outlined in Figure 3.19. Of the 36 points collected, 24 points were examined immediately around the impact zone to measure the residual stress state. The resulting peak center and shift was observed to be quite uniform.

The two additional panels, with either CSR and CNT micro particles, were scanned with the modified methodology presented in Figure 3.20 due to the high levels of background fluorescence. Increased background intensity diminished the ability to distinguish the peaks, which limited the data points able to be collected. 8 points were able to be utilized, packed in a small region to the lower left of the impact zone. The findings

showed a marked difference on the Raman response as compared to the baseline ballistic panel due to both of the additives. The resulting peak centers and standard deviation are presented in Table 6.2 with the literature comparison from Cen et al. [20]

Table 6.2: Resulting Peak Centers for Pristine, Literature, Baseline, and Additive Panels with Statistical Data

Sample	**Pristine**	**Cen et al.**	**Baseline**	**CSR**	**CNT**
Peak A Center	1610.942	1611	1609.875	1611.22	1609.52
Standard Dev.: Peak A	0.098	NA	0.179	0.279	0.755
Shift from Pristine	**0**	**-0.058**	**1.066**	**-0.278**	**1.422**
Peak B Center	1648.512	NA	1647.213	1647.845	1647.991
Standard Dev.: Peak B	0.3	NA	0.66	0.809	0.421
Shift from Pristine	**0**	**NA**	**1.299**	**0.667**	**0.52**

The findings from the piezospectroscopic study of the baseline and additive panels were quite unexpected. The additives' Raman response was compared to their ballistic performance, where the CSR additive improved ballistic performance by 8% and the CNT additive improved performance by 7.3%. The expectation was that the additive panels Raman results would show a similar shift in peak center, with a marked difference from the baseline. However, the true findings showed that the Raman response for the primary band at 1611 cm^{-1} had an upshift for the CSR panel and a downshift for the CNT panel , as compared to the baseline panel. The response for the secondary band at

1648 cm^{-1} both has slight upshifts as compared with the baseline panel. The findings are presented in a bar graph in Figure 6.4 for clarity.

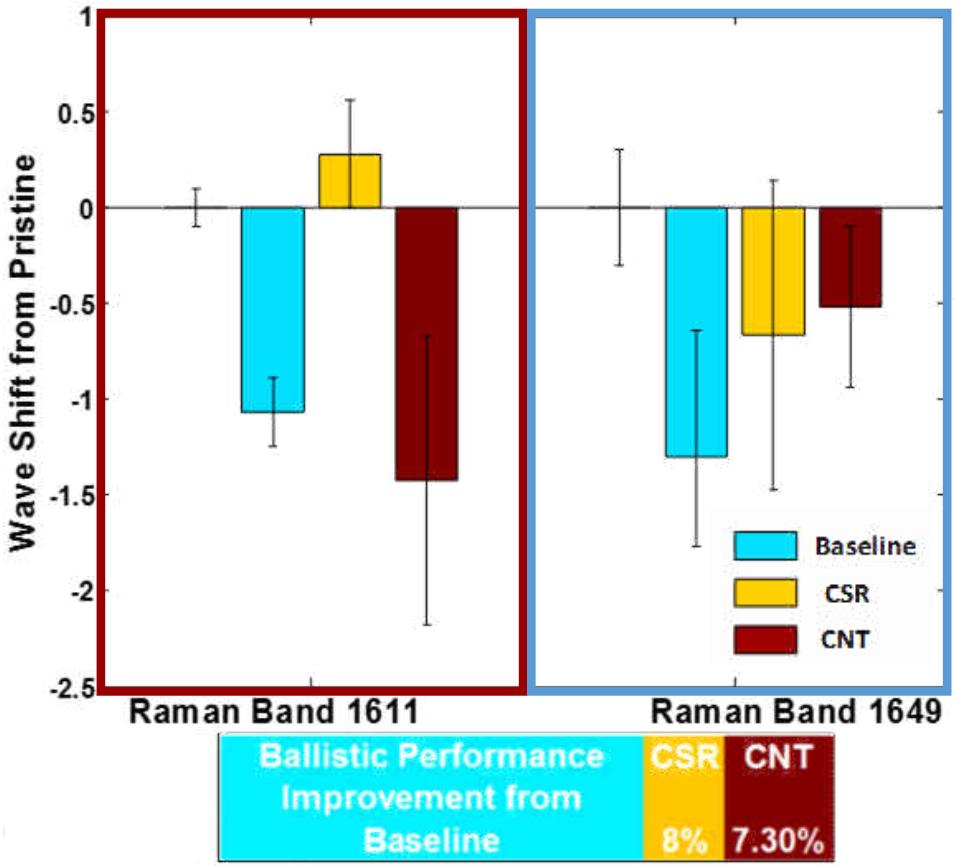

Figure 6.4: Additive's Effect on Piezospectoscopy Compared with Ballistic Resistance Performance

Interestingly, the CNT appears to allow for the Kevlar® fibers to experience greater axial stress than the baseline panel. This may account for part of the increase in ballistic

resistance. It can be suggested that this is due from influence of the nano-tubes on the Kevlar® fibers, and how they run parallel to the fiber's length. Conversely, the CSR panel experience less axial stress in comparison with the baseline, yet with greater ballistic performance. This is attributed to the nano-particle dispersed in the epoxy resin matrix, where cavitation may impede the damage propagation and absorb a great deal of energy.

Comparing the secondary band's results, it can be observed that both additives result in a reduction of the internal radial stress of the fiber, as seen in the peak up-shift. This suggests that the additives are absorbing part of the energy wave as it sweeps through the composite weave, whereby protecting the Kevlar® fibers from the tearing radial stress.

6.4 Conclusions

The CSR nano-particle additive appears to be more effective in reducing the force experienced by the Kevlar® fibers, while providing a marked improvement in ballistic performance. CNT additives appear to focus the loads in the direction the fibers are oriented and reduce the loads that result in the fibers tearing. It too provided a marked improvement in ballistic performance. For future consideration, both additives in conjunction should be implemented to the baseline composite to test for further increases in ballistic performance. This is likely, as the additives appear to have different effects on the damage mechanisms and the material response to dynamic loading. Due to their

minimal weight additions and likelihood for great increases in ballistic performance, this further testing is planned in the future work.

CHAPTER 7
CONCLUSIONS AND FUTURE OUTLOOK

Throughout this study, nondestructive techniques have been used to investigate material behavior and damage mechanisms for aerospace materials. The techniques of piezospectroscopy and synchrotron radiation worked well in conjunction with one another to shed light onto the material's characteristics.

In Chapter 4, piezospectroscopic testing techniques were able to perform phase and constituent identification and shed light on the response to loading conditions. It was found that the development of the thermally grown oxide, under varying thermal loads, is non-uniform and subject to high stress gradients over small distances. Stress maps revealed a 0.5 GPa stress variation in response to small changes in thermal loading. Variations in the oxide layer's development and stress profile were observed to have marked effects on the thermal barrier coating system. Aging of the specimen over long duration was shown to unify the stress profile for both the thermally grown oxide and the zirconia top coat. The aged oxide presented a decrease in stress in comparison to the early cycled aged specimen, due to growth and development with its highest stress value being during early stages of growth. Micro damage was observed in the thermally grown oxide, revealing the initiation of damage due to the aging process. These zones were seen to have an effect on the attached coating around them. The findings also suggest that long duration aging under dynamic and varying loading conditions may establish stress

profile variations that lead to changes in material response, damage propagation, and failure mechanics.

In Chapter 5, X-Ray diffraction measurements afforded an investigation into the strain response of both the bond coat and top coat of the thermal barrier coating system with the high energy radiation afforded by the synchrotron. The piezospectroscopy studies validated that the scanning location of the diffraction measurements, as the region was nearly uniform in thermal loading and the thermally grown oxide's development. Effects due to thermal loading during the representative cycle are evident from the diffraction studies of multiple constituents and crystallographic planes. At room temperature, both the bond coat and top coat phases showcase a high residual strain due to the thermal expansion mismatch from the coating temperature to the ambient. Upon returning to high temperature the strain state is reduced, and the bond coat is observed to change from compressive to slightly tensile for e_{11} and tensile to slightly compressive. The zirconia showed a reduction of compressive strain to near zero during high temperature as well. Anisotropic effects are also observed by measuring the strain in multiple crystallographic planes, and deviation due to changes in temperatures was noted. These results can be used to advance and validate material response models as transient trends were able to be observed. The findings showcase the necessity and challenge of incorporating complex realistic geometry and representative service loads and aging conditions.

In Chapter 6 piezospectroscopic studies on Kevlar® ballistic panels shed light on the load transfer and damage propagation mechanics for fiber composites. Performance

enhancing additives were compared for their ballistic performance and their effect on the Raman response. It is suggested that the additives are absorbing part of the energy wave in response to impact loads as it sweeps through the composite weave, whereby protecting the Kevlar® fibers from the tearing radial stress. The CSR nanoparticle additive appears to be more effective in reducing the force transfered to the Kevlar® fibers, while providing a marked improvement in ballistic performance. CNT additives appear to focus the loads in the direction the fibers and reducing the loads that result in the fibers tearing.

The CNT additive appears to allow for the Kevlar® fibers to experience greater axial stress than the baseline panel. This may account for part of the increase in ballistic resistance. It can be suggested that this is due from influence of the nanotubes on the Kevlar® fibers, and how they run parallel to the fiber's length. Conversely, the CSR panel experience less axial stress in comparison with the baseline, yet with greater ballistic performance. This is attributed to the nanoparticle dispersed in the epoxy resin matrix, where cavitation may impede the damage propagation and absorb a great deal of energy.

Future work will provide piezospectroscopic and diffraction studies on thermal barrier coated samples with different stages of aging, for additional investigations into the effects of long duration under complex loading. Samples near their end of life failure modes will be considered to demonstrate how a lifetime of non-uniform loading conditions influences the failure behavior. Of particular interest is the study of the influence of cooling holes,

their role on the stress field's development, and understanding their influence of damage mechanisms. A combination of additives will be introduced to the Kevlar® ballistic composites to test for further increases in ballistic performance with minimum weight addition, and to better understand how the additives influence damage mechanisms and the material response to dynamic loading by means of Raman spectroscopy. Additional scanning parameters will be tested to provide high resolution stress contour maps of the ballistic impact site to better map the response to damage by the composite.

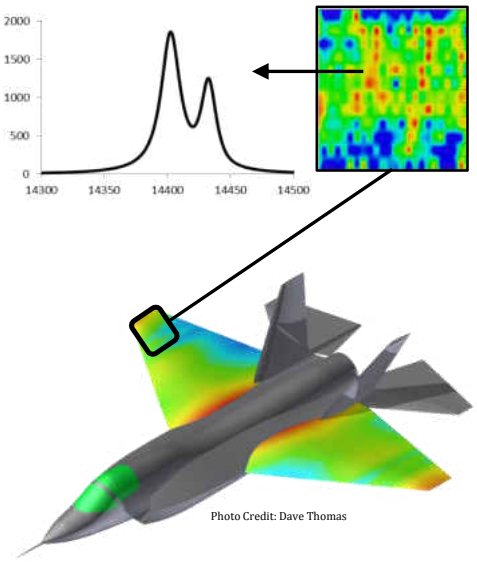

Figure 7.1: Application of Customized Stress and Damage Sensitive Composite Coatings for Use in Non-Destructive Testing of Aerospace Vehicles. [54] *Image Credit*: *Dave Thomas*

The success of these nondestructive testing techniques and their effectiveness to investigating damage mechanisms and material response on a variety of aerospace materials allows for more rapid characterization of novel composites for application in aerospace environments and additional fields. An area of work to be investigated is incorporating nano-scale additives into coatings for the development of smart sensor as described in Figure 7.1. Applications of these smart sensors and remote portable testing are very exciting for the fields of aerospace, structural health monitoring, and remotely identifying damage in hostile environments of which it is costly or not feasible to send an inspection team.

LIST OF REFERENCES

[1] J. Almer, U. Lienert, R. L. Peng, C. Schlauer, and M. Oden. Strain and texture analysis of coatings using high energy xrays. *Journal of Applied Physics*, 94:697–702, 2003.

[2] J. Almer and S. Stock. Internal strains and stresses measured in cortical bone via high-energy X-Ray diffraction. *Journal of Structural Biology*, 152:14–27, 2005.

[3] J. Almer, G. Swift, J. Nychka, E. Ustundag, and D. Clarke. In situ synchrotron measurements of oxide growth strains. *Materials Science Forum*, 490-491:287–293, 2005.

[4] D. Balint and J. Hutchinson. An analytical model of rumpling in thermal barrier coatings. *Journal of the Mechanics and Physics of Solids*, 53:949–793, 2005.

[5] D. Bannister, M. Andrews, A. Cervenka, and R. Young. Analysis of the single-fibre pull-out test by means of raman spectroscopy: Part *ii*. micromechanics of deformation for an aramid/epoxy system. *Composites science and technology*, 53(4):411–421, 1995.

[6] C. N. Banwell and E. M. McCash. *Fundamentals of Molecular Spectroscopy*. McGraw-Hill London, 1983.

[7] E. Bartsch, B. Baufeld, S. Dalkili, I. Mircea, K. Lambrinou, T. Leist, J. Yan, and A. M. Karlsson. Time-economic lifetime assessment for high performance thermal barrier coating systems. *Key Engineering Materials*, 333:147–145, 2007.

[8] M. Bartsch, B. Baufeld, S. Dalkili, and I. Mircea. Testing and characterization of ceramic thermal barrier coatings. *Materials Science Forum*, 492-493:3–8, 2005.

[9] M. Bartsch, B. Baufeld, S. Dalkilic, L. Chernova, and M. Heinzelmann. Fatigue cracks in a thermal barrier coating system on a superalloy in multiaxial thermomechanical testing. *International Journal of Fatigue*, 30:211218, 2008.

[10] W. W. Bathie. Fundamentals of gas turbines. 1984.

[11] C. Baudín, J. Gurauskis, A. J. Sánchez-Herencia, and V. M. Orera. Indentation damage and residual stress field in alumina-Y2O3-stabilized zirconia composites. *Journal of the American Ceramic Society*, 92(1):152–160, 2009.

[12] H. Bhatnagar, S. Ghosh, and M. E. Walter. Parametric studies of failure mechanisms in elastic EBPVD thermal barrier coatings using fem. *International Journal of Solids and Structures*, 43:4384–4406, 2006.

[13] J. Blitz. *Electrical and magnetic methods of non-destructive testing*, volume 3. Springer, 1997.

[14] A. Bolcavage, A. Feuerstein, J. Foster, and P. Moore. Thermal shock testing of tbc bondcoat systems. *Journal of Materials Engineering and Performance*, 13:389–397, 2004.

[15] G. Breitbach and F. Schubert. A contribution to stress prediction in coatings for gas turbine blades. *Archive of Applied Mechanics*, 73:682–689, 2004.

[16] H. Brodin, M. Jinnestraud, S. Johansson, and S. Sjostrom. Thermal barrier coating fatigue life assessment. Technical report, Siemens AG, 2006.

[17] J. Cai, Y. Raptis, and E. Anastassakis. Stabilized cubic zirconia: A Raman study under uniaxial stress. *Applied physics letters*, 62(22):2781–2783, 1993.

[18] N. Carlson and B. L. Stoner. Thermal barrier coating on high temperature industrial gas turbine engines. *Final Report United Technologies Corp., South Windsor, CT. Power Systems Div.*, 1, 1977.

[19] P. Cawley and R. D. Adams. A vibration technique for non-destructive testing of fibre composite structures. *Journal of Composite Materials*, 13(2):161–175, 1979.

[20] H. Cen, Y. Kang, Z. Lei, Q. Qin, and W. Qiu. Micromechanics analysis of Kevlar29 aramid fiber and epoxy resin microdroplet composite by micro-raman spectroscopy. *Composite structures*, 75(1):532–538, 2006.

[21] M. Chambers and D. R. Clarke. Effect of long term, high temperature aging on luminescence from Eu-doped YSZ thermal barrier coatings. *Surface and Coatings Technology*, 201(7):3942–3946, 2006.

[22] H. Chen, X. Zhou, and C. Ding. Investigation of the thermomechanical properties of a plasma-sprayed nanostructured zirconia coating. *Journal of the European Ceramic Society*, 23(9):1449–1455, 2003.

[23] W. Chen and H. Luo. Dynamic compressive responses of intact and damaged ceramics from a single split hopkinson pressure bar experiment. *Experimental Mechanics*, 44 No. 3:295–299, 2004.

[24] W. Chen, X. Wu, B. Marple, and P. Patnaik. The growth and influence of thermally grown oxide in a thermal barrier coating. *Surface Coatings and Technology*, 201:1074–1079, 2006.

[25] J. Cheng, E. Jordan, B. Barber, and M. Gell. Thermal residual stress in an electron beam physical vapor deposited thermal barrier coating system. *Acta Materialia*, 46(16):5839 – 5850, 1998.

[26] R. Christensen, D. Lipkin, and D. Clarke. Nondestructive evaluation of the oxidation stresses through thermal barrier coatings using Cr^{3+} piezospectroscopy. *Applied Physics Letters*, 69:3754–3756, 1996.

[27] M. Clark, D. McCann, and M. Forde. Application of infrared thermography to the non-destructive testing of concrete and masonry bridges. *Ndt & E International*, 36(4):265–275, 2003.

[28] H. Cole. Bragg's law and energy sensitive detectors. *Journal of Applied Crystallography*, 3(5):405–406, 1970.

[29] P. Costamagna, L. Magistri, and A. Massardo. Design and part-load performance of a hybrid system based on a solid oxide fuel cell reactor and a micro gas turbine. *Journal of Power Sources*, 96(2):352–368, 2001.

[30] P. M. Cunniff. A semiempirical model for the ballistic impact performance of textile-based personnel armor. *Textile Research Journal*, 66(1):45–58, 1996.

[31] N. Czech and S. Chandra. Trends in developing coatings for gas turbine applications. In *The Future of Gas Turbine Technology"*. NCConsulting, 2008.

[32] R. J. Davies, M. Burghammer, and C. Riekel. Simultaneous microraman and synchrotron radiation microdiffraction: Tools for materials characterization. *Applied Physics Letters*, 87:264105, 2005.

[33] C. Dawes, H. Reichard, and P. Humphries. Abridgment of ionization studies in paper insulated cables–II. *AIEE, Journal of the*, 48(1):3–7, 1929.

[34] G. de Portu, L. Micele, Y. Sekiguchi, and G. Pezzotti. Measurement of residual stress distributions in Al2O3/3Y-TZP multilayered composites by fluorescence and raman microprobe piezo-spectroscopy. *Acta Materialia*, 53:1511–1520, 2005.

[35] J. T. DeMasi, K. D. Sheffler, and M. Ortiz. Thermal barrier coating life prediction model development. phase *I* - final report. Technical Report CR-182230, UNITED TECHNOLOGIES CORPORATION Pratt & Whitney Commercial Engine Business, December 1989. Prepared for National Aeronautics and Space Administration Under Contract NAS3-23944.

[36] R. Diaz, M. Jansz, M. Mossaddad, S. Raghavan, J. Okasinski, J. Almer, H. Pelaez-Perez, and P. Imbrie. Role of mechanical loads in inducing in-cycle tensile stress in thermally grown oxide. *Applied Physics Letters*, 100(11):111906, 2012.

[37] R. O. Diaz. In-situ stress measurements of eb-pvd thermal barrier coatings using synchrotron X-Ray diffraction under thermo-mechanical loading. Master's thesis, University of Central Florida, 2010.

[38] J. W. Downing and J. A. Newell. Characterization of structural changes in thermally enhanced kevlar-29 fiber. *Journal of applied polymer science*, 91(1):417–424, 2004.

[39] Z. A. Dreger and Y. M. Gupta. Raman spectroscopy of high-pressure, high-temperature polymorph of hexahydro-1,3,5-trinitro-1,3,5-triazine (ϵ-rdx). *J. Phys. Chem. A*, 114:7038–7047, 2010.

[40] J. M. Drexler, A. Aygun, D. Li, R. Vaben, T. Steinke, and N. P. Padture. Thermal-gradient testing of thermal barrier coatings under simultaneous attack by molten glassy deposits and its mitigation. *Surface and Coatings Technology*, 204:2683–2688, 2010.

[41] Y. Duan, M. Keefe, T. Bogetti, and B. Cheeseman. Modeling friction effects on the ballistic impact behavior of a single-ply high-strength fabric. *International Journal of Impact Engineering*, 31(8):996–1012, 2005.

[42] H. Dunegan and D. Harris. Acoustic emission-a new nondestructive testing tool. *Ultrasonics*, 7(3):160–166, 1969.

[43] DuPont. *Kevlar Technical Guide, H-77848 4/00;*, 2000.

[44] W. A. Ellingson, R. J. Visher, R. S. Lipanovich, and C. M. Deemer. Optical ndt methods for ceramic thermal barrier coatings. *Materials evaluation*, 64(1):45–51, 2006.

[45] A. G. Evans, D. R. Clarke, and C. G. Levi. The influence of oxides on the performance of advanced gas turbines. *Journal of the European Ceramic Society*, 28:1405–1419, 2008.

[46] A. G. Evans, M. Y. He, A. Suzuki, M. Gigliotti, B. Hazel, and T. M. Pollock. A mechanism governing oxidation-assisted low-cycle fatigue of superalloys. *Acta Materialia*, 57:2969 – 2983, 2009.

[47] H. Evans. Oxidation failure of tbc systems: An assessment of mechanisms. *Surface and Coatings Technology*, 206(7):1512 – 1521, 2011.

[48] T. Field, A. Jones, M. Jansz, S. Raghavan, J. Okasinski, and J. Almer. Synchrotron x-rays monitoring nano-aluminum grain growth of a metal matrix composite under thermo-mechanical conditions. In *53rd AIAA/ASME/ASCE/AHS/ASC Structures, Structural Dynamics and Materials Conference 20th AIAA/ASME/AHS Adaptive Structures Conference 14th AIAA*, 2012.

[49] M. Fitzpatrick, A. Fry, P. Holdway, F. Kandil, J. Shackleton, and L. Suominen. Determination of residual stresses by X-Ray diffraction. 2005.

[50] M. M. Gentleman, V. Lughi, J. A. Nychka, and D. R. Clarke. Noncontact methods for measuring thermal barrier coating temperatures. *International journal of applied ceramic technology*, 3(2):105–112, 2006.

[51] J. Gibson, J. McKee, G. Freihofer, S. Raghavan, and J. Gou. Enhancement in ballistic performance of composite hard armor through carbon nanotubes. *International Journal of Smart and Nano Materials*, (ahead-of-print):1–17, 2014.

[52] L. Grabner. Spectroscopic technique for the measurement of residual stress in sintered Al2O3. *Journal of Applied Physics*, 49(5):580–583, 1978.

[53] Y. Gupta and X. Shen. Potential use of the ruby R2 line shift for static highpressure calibration. *Applied Physics Letters*, 58:583–585, 1991.

[54] W. Gysi, K. Lautenslager, G. Freihofer, A. Jones, C. Jollivet, A. Schülzgen, and S. Raghavan. Stress-sensing nanomaterials using photo-stimulated luminescence spectroscopy. *The Showcase of Undergraduate Research of the University of Central Florida*, 2012.

[55] B. He. Introduction to two dimensional xray diffraction. *Powder Diffraction*, 18(2):71–85, June 2003.

[56] B. B. He. *Two-dimensional X-ray Diffraction*. John Wiley & Sons, 2011.

[57] M. He, J. Hutchinson, and A. Evans. Large deformation simulations of cyclic displacement instabilities in thermal barrier systems. *Acta Materialia*, 50:1063–1073, 2002.

[58] U. Hermosilla. *Mechanical Modelling Of Thermal Barrier Coatings At High Temperatures*. PhD thesis, University of Nottingham, 2008.

[59] M. T. Hernandez, D. Cojocaru, M. Bartsch, and A. M. Karlsson. On the opening of a class of fatigue cracks due to thermo-mechanical fatigue testing of thermal barrier coatings. *Computational Materials Science*, 50:2561–2572, 2011.

[60] M. T. Hernandez, A. M. Karlsson, and M. Bartsch. On tgo creep and the initiation of a class of fatigue cracks in thermal barrier coatings. *Surface Coatings and Technology*, 203:3549–3558, 2009.

[61] R. Hillery, B. Pilsner, R. McKnight, T. Cook, and M. Hartle. Thermal barrier coating life prediction model development. Technical report, NASA, 1988.

[62] P. Y. Hou, A. P. Paulikas, and B. W. Veal. Growth strains and stress relaxation in alumina scales during high temperature oxidation. In *6th Symposium on High Temperature Corrosion and Protection of Materials*, 2004.

[63] D. C. J.A. Nychka. Damage quantification in TBCs by photo-stimulated luminescence spectroscopy. *Surface Coatings and Technology*, 146-147:110–116, 2001.

[64] J. Kaczmar, K. Pietrzak, and W. Włosiński. The production and application of metal matrix composite materials. *Journal of Materials Processing Technology*, 106(1):58–67, 2000.

[65] Y. Kadioglu and H. Sehitoglu. Thermomechanical and isothermal fatigue behavior of bare and coated superalloys. *Transactions of the ASME*, 117:94–102, 1995.

[66] M. Karadge, X. Zhao, M. Preuss, and P. Xiao. Microtexture of the thermally grown alumina in commercial thermal barrier coatings. *Scripta Materialia*, 54:639–644, 2006.

[67] A. M. Karlsson and A. G. Evans. A numerical model for the cyclic instability of thermally grown oxides in thermal barrier systems. *Acta Materialia*, Volume 49 Issue 10:1793–1804, 2001.

[68] A. M. Karlsson, J. W. Hutchinson, and A. G. Evans. A fundamental model of cyclic instabilities in thermal barrier systems. *Journal of the Mechanics and Physics of Solids*, 50:1565–1589, 2002.

[69] P. Kim, C. Chang, and S. Hsu. Normal vibrational analysis of a rigid rod polymer: poly-(p-phenylene terephthalamide). *Polymer*, 27(1):34–46, 1986.

[70] K. Knipe, A. Maneo, S. F. Siddiqui, C. Meid, J. Wischek, J. Okasinski, J. Almer, M. Bartsch, and S. Raghavan. Strain reponse of thermal barrier coatings captured under extreme engine environments through synchrotron X-Ray diffraction. *In Review*.

[71] K. Knipe, A. Manero, S. F. Siddiqui, S. Sofronsky, P. Fouquet, S. Raghavan, C. Meid, J. Wischek, M. Bartsch, J. Okasinski, et al. Synchrotron XRD measurements of thermal barrier coatings subjected to loads representing operational conditions of rotating gas turbine blades.

[72] A. Korsunsky, K. E. Wells, and P. Withers. Mapping two dimensional state of strain using synchrotron X-ray diffraction. *Scripta Materialia*, 39:1705–1712, 1998.

[73] B. Kramer et al. *Einheiten und Fundamentalkonstanten in Physik und Chemie*, volume 1. Springer, 1992.

[74] R. Krishnan. Raman spectrum of alumina and the luminescence of ruby. In *Proceedings of the Indian Academy of Sciences*, volume 26 of *A*, pages 450–459, Department of Physics, Indian Institute of Science, Bangalore, November 1947. The Bangalore Press.

[75] J. Lankford, W. Predebon, J. Staehler, G. Subhash, B. Pletka, and C. Anderson. The role of plasticity as a limiting factor in the compressive failure of high strength ceramics. *Mechanics of Materials*, 29:205–218, 1998.

[76] C. H. Leibert and S. Stecura. Thermal barrier coating system, Oct. 25 1977. US Patent 4,055,705.

[77] C. H. Liebert, R. Jacobs, S. Stecura, and C. Morse. Durability of zirconia thermal-barrier ceramic coatings on air-cooled turbine blades in cyclic jet engine operation. Technical report, National Aeronautics and Space Administration, Cleveland, OH (USA). Lewis Research Center, 1976.

[78] A. M. Limarga and D. R. Clarke. Piezo-spectroscopic coefficients of tetragonal-prime yttria-stabilized zirconia. *Journal of the American Ceramic Society*, 90(4):1272–1275, 2007.

[79] A. M. Limarga, R. Vaßen, and D. R. Clarke. Stress distributions in plasma-sprayed thermal barrier coatings under thermal cycling in a temperature gradient. *Journal of Applied Mechanics*, 78(1):011003, 2011.

[80] D. Lipkin and D. Clarke. Sample-probe interactions in spectroscopy: Sampling microscopic property gradients. *Journal of Applied Physics*, 77:1855–1863, 1995.

[81] D. Liu, O. Lord, and P. E. Flewitt. Calibration of Raman spectroscopy in the stress measurement of air-plasma-sprayed yttria-stabilized zirconia. *Applied spectroscopy*, 66(10):1204–1209, 2012.

[82] F. Liu and W. A. Sirignano. Turbojet and turbofan engine performance increases through turbine burners. *Journal of Propulsion and Power*, 17(3):695–705, 2001.

[83] V. Lughi and D. R. Clarke. High temperature aging of YSZ coatings and subsequent transformation at low temperature. *Surface and Coatings Technology*, 200(5):1287–1291, 2005.

[84] V. Lughi and D. R. Clarke. Transformation of electron-beam physical vapor-deposited 8 wt% yttria-stabilized zirconia thermal barrier coatings. *Journal of the American Ceramic Society*, 88(9):2552–2558, 2005.

[85] V. Lughi, V. K. Tolpygo, and D. R. Clarke. Microstructural aspects of the sintering of thermal barrier coatings. *Materials Science and Engineering: A*, 368(1):212–221, 2004.

[86] Y. Maniwa, R. Fujiwara, H. Kira, H. Tou, H. Kataura, S. Suzuki, Y. Achiba, E. Nishibori, M. Takata, M. Sakata, et al. Thermal expansion of single-walled carbon nanotube (SWNT) bundles: X-ray diffraction studies. *Physical Review B*, 64(24):241402, 2001.

[87] W. Mao, Q. Chen, C. Dai, L. Yang, Y. Zhou, and C. Lu. Effects of piezo-spectroscopic coefficients of 8wt.% Y2O3 stabilized ZrO2 on residual stress measurement of thermal barrier coatings by raman spectroscopy. *Surface & Coatings Technology*, 204(21):3573, 2010.

[88] G. Marsh. Composites lift off in primary aerostructures. *Reinforced plastics*, 48(4):22–27, 2004.

[89] A. F. Massardo, C. F. McDonald, and T. Korakianitis. Microturbine/fuel-cell coupling for high-efficiency electrical-power generation. *Journal of Engineering for Gas Turbines and Power*, 124(1):110–116, 2002.

[90] K. L. McNesby, J. E. Wolfe, J. B. Morris, and R. A. Pesce-Rodriguez. FT-Raman spectroscopy of some energetic materials and propellant formulations. *Army Research Laboratory*, 233:1–38, 1993.

[91] P. E. Mix. *Introduction to nondestructive testing: a training guide*. John Wiley & Sons, 2005.

[92] S. E. Molis and D. R. Clarke. Measurement of stresses using fluorescence in an optical microprobe: Stresses around indentations in a chromium-doped sapphire. *Journal of Electronic Structure of Ceramics*, 73(11):3189 –3194, 1990.

[93] M. T. Naeem, S. A. Jazayeri, and N. Rezamahdi. Failure analysis of gas turbine blades. In *Proceedings of The 2008 IAJC-IJME International Conference*, 2009.

[94] K. Nakamoto. *Infrared and Raman spectra of inorganic and coordination compounds*. Wiley Online Library, 1978.

[95] J. Nicholls and R. Wellman. Erosion and foreign object damage of thermal barrier coatings. In *RTO AVT Specialists Meeting on "The Control and Reduction of Wear in Military Platforms"*. RTO, June 2004.

[96] J. A. Nychka and D. R. Clarke. Damage quantification in TBCs by photo-stimulated luminescence spectroscopy. *Surface Coatings and Technology*, 146-147:110–116, 2001.

[97] H. Ohnabe, S. Masaki, M. Onozuka, K. Miyahara, and T. Sasa. Potential application of ceramic matrix composites to aero-engine components. *Composites Part A: Applied Science and Manufacturing*, 30(4):489–496, 1999.

[98] N. P. Padture, M. Gell, and E. H. Jordan. Thermal barrier coatings for gas-turbine engine applications. *Science*, 296:280–284, 2002.

[99] B. Parga-Landa and F. Hernandez-Olivares. An analytical model to predict impact behaviour of soft armours. *International Journal of Impact Engineering*, 16(3):455–466, 1995.

[100] A. Peichl, T. Beck, and O. Vohringer. Behavior of an EB-PVD thermal barrier caoting system under thermal-mechanical fatigue loading. *Surface Coatings and Technology*, 162:113–118, 2003.

[101] L. Penn and F. Milanovich. Raman spectroscopy of kevlar 49 fibre. *Polymer*, 20(1):31–36, 1979.

[102] J. Petek and P. Hamilton. Performance monitoring for gas turbines performance monitoring for gas turbines. *Orbit*, 75:64–74, 2005.

[103] J. Quintanilla. Microstructure and properties of random heterogeneous materials: A review of theoretical results. *Polymer Engineering & Science*, 39(3):559–585, 1999.

[104] J. Robin. Raman microscopy: application to the identification of pigments on medieval manuscripts. *Chemical Society Reviews*, 24(3):187–196, 1995.

[105] J. Rösler, M. Bäker, and K. Aufzug. A parametric study of the stress state of thermal barrier coatings: part i: creep relaxation. *Acta materialia*, 52(16):4809–4817, 2004.

[106] J. Rosler, B. M., and M. Volgmann. Stress state and failure mechanisms of thermal barrier coatings: Role of creep in thermally grown oxide. *Acta Materialia*, 49:3659–3670, 2001.

[107] R. L. Sanford. Non-destructive testing of steel hoisting rope. *Mining and Metallurgy*, 4(199), 1923.

[108] S. Saunders, J. Banks, G. Chen, and C. Chunnilal. Measurement of residual stress in thermally grown oxide layers in thermal barrier coating systems - development of non-destructive test methods. *Materials Science Forum*, 461-464:383–390, 2004. .pdf ok.

[109] U. Schulz, C. Leyens, K. Fritscher, M. Peters, B. Saruhan-Brings, O. Lavigne, J.-M. Dorvaux, M. Poulain, R. Mévrel, and M. Caliez. Some recent trends in research and technology of advanced thermal barrier coatings. *Aerospace Science and Technology*, 7:73–80, 2003.

[110] A. Scrivani, G. Rizzi, U. Bardi, C. Giolli, M. M. Miranda, S. Ciattini, A. Fossati, and F. Borgioli. Thermal fatigue behavior of thick and porous thermal barrier coatings systems. *Journal of Thermal Spray Technology*, 16:816821, 2007.

[111] V. Sergo, D. R. Clarke, and W. Pompe. Deformation bands in ceria-stabilized tetragonal zirconia/alumina: I, measurement of internal stresses. *Journal of the American Ceramic Society*, 78(3):633–640, 1995.

[112] K. D. Sheffler and D. K. Gupta. Current status and future trends in turbine application of thermal barrier coatings. *Journal of Engineering for Gas Turbines and Power*, 110(4):605–609, 1988.

[113] J. Shi, A. M. Karlsson, B. Baufeld, and M. Bartsch. Evolution of surface morphology of thermo-mechanically cycled nicocraly bond coats. *Materials Science and Engineering*, 434:39–52, 2006.

[114] S. F. Siddiqui, K. Knipe, A. Manero, C. Meid, J. Wischek, J. Okasinski, J. Almer, A. M. Karlsson, M. Bartsch, and S. Raghavan. Synchrotron X-Ray measurement techniques for thermal barrier coated cylindrical samples under thermal gradients. *Review of Scientific Instruments*, 84(8):083904, 2013.

[115] B.-H. Sjostrom, S. Influence of tbc end geometry on the TMF life of an aps tbc. *Procedia Engineering*, 2:1363–1371, 2010.

[116] W. Skorotzki, B. Kloden, R. Tamm, C. G. Oertel, U. Garbe, and E. Rybacki. Torsion texture measurements with high energy synchrotron radiation on nial. *Textures and Microstructures*, 35:163–173, 2003.

[117] S.Margueron and D. Clarke. Effect of residual stress on the luminescence lifetime of r-line emission from polycrystalline alumina formed by oxidation. *Journal of the American Ceramic Society*, 90:1798–1801, 2007.

[118] S. Sridharan, L. Xie, E. H. Jordan, and M. Gell. Stress variation with thermal cycling in the thermally grown oxide of an eb-pvd thermal barrier coating. *Surface Coatings and Technology*, 179:286–296, 2004.

[119] V. T. Srikar, A. K. Swan, M. S. Unlu, B. B. Goldberg, and S. M. Spearing. Micro-Raman measurement of bending stresses in micromachined silicon flexures. *Journal of Microelectromechanical Systems*, 12:779–787, 2003.

[120] A. Steuwer, J. R. Santisteban, M. Turski, P. J. Withers, and T. Buslaps. High-resolution strain mapping in bulk samples using full-profile analysis of energy-dispersive synchrotron X-Ray diffraction data. *Journal of Applied Crystallography*, 37:883–889, 2005.

[121] A. Stevenson. Calibration of alumina-epoxy nanocomposites using piezospectroscopy for the development of stress-sensing adhesives. Master's thesis, University of Central Florida, 2011.

[122] A. Stevenson, A. Jones, and S. Raghavan. Stress-sensing nanomaterial calibrated with photostimulated luminescence emission. *Nano Letters*, 11:3274–3278, 2011.

[123] K. Suzuki, T. Shobu, and K. Tanaka. Residual stresses of ebpvd thermal barrier coatings exposed to high temperature. *International Center for Diffraction Data*, ISSN 1097-0002:537–544, 2009.

[124] M. Tanaka, R. Kitazawa, T. Tomimatsu, Y. Liu, and Y. Kagawa. Residual stress measurement of an EB-PVD Y2O3-ZrO2 thermal barrier coating by micro-Raman spectroscopy. *Surface & Coatings Technology*, 204:657–660, 2009.

[125] M. Tanaka, C. Mercer, Y. Kagawa, and A. G. Evans. Thermomechanical fatigue damage evolution in a superalloy/thermal barrier system containing a circular through hole. *Journal of American Ceramic Society*, 94 [S1]:S128–S135, 2011.

[126] V. Teixeira, M. Andritschky, W. Fischer, H. Buchkremer, and D. Stöver. Analysis of residual stresses in thermal barrier coatings. *Journal of Materials Processing Technology*, 92:209–216, 1999.

[127] T. Thomas. Fundamentals of Raman Spectroscopy. Technical report, BWTEK INC, 2012.

[128] J. Thornton, S. Slater, and J. Almer. The measurement of residual strains within thermal barrier coatings using high-energy X-Ray diffraction. *Journal of the American Ceramic Society*, 88:2817–2825, 2005.

[129] V. Tolpygo, D. Clarke, and K. Murphy. Oxidation-induced failure of EB-PVD thermal barrier coatings. *Surface and Coatings Technology*, 146:124–131, 2001.

[130] T. Tomimatsu, Y. Kagawa, and S. Zhu. Residual stress distribution in electron beam-physical vapor deposited ZrO2 thermal barrier coating layer by raman spectroscopy. *Metallurgical and Materials Transactions A*, 34(8):1739–1741, 2003.

[131] J. Toscano, D. Naumenko, A. Gil, L. Singheiser, and W. Quadakkers. Parameters affecting tgo growth rate and the lifetime of TBC systems with mcraly-bondcoats. *Materials and corrosion*, 59(6):501–507, 2008.

[132] G. Ventura and V. Martelli. Thermal conductivity of kevlar 49 between 7 and 290k. *Cryogenics*, 49(12):735–737, 2009.

[133] X. Wang, G. Lee, and A. Atkinson. Investigation of TBCs on turbine blades by photoluminescence piezospectroscopy. *Acta Materialia*, 57(1):182–195, 2009.

[134] G. Washer, T. Brooks, and R. Saulsberry. Characterization of kevlar using raman spectroscopy. *Journal of Materials in Civil Engineering*, 21(5):226–234, 2009.

[135] P. Withers and P. Webster. Neutron and synchrotron X-Ray strain scanning. *Strain*, 37(1):19–33, 2001.

[136] H. Wu, S. Roberts, G. Mobus, and B. Inkson. Subsurface damage analysis by tem and 3D FIB crack mapping in alumina and alumina/5vol.% SiC nanocomposites. *Acta Materialia*, 51:149–163, 2003.

[137] M. Yashima, N. Ishizawa, and M. Yoshimura. High-temperature X-Ray study of the cubic-tetragonal diffusionless phase transition in the ZrO2- ErO1.5 system: I, phase change between two forms of a tetragonal phase, t'-ZrO2 and t "-ZrO2, in the compositionally homogeneous 14 mol% ErO1. 5-ZrO2. *Journal of the American Ceramic Society*, 76(3):641–648, 1993.

[138] M. Yashima, S. Sasaki, M. Kakihana, Y. Yamaguchi, H. Arashi, and M. Yoshimura. Oxygen-induced structural change of the tetragonal phase around the tetragonal-cubic phase boundary in ZrO2-YO1.5 solid solutions. *Acta Crystallographica Section B: Structural Science*, 50(6):663–672, 1994.

[139] M. Yashima, S. Sasaki, Y. Yamaguchi, M. Kakihana, M. Yoshimura, and T. Mori. Internal distortion in ZrO2–CeO2 solid solutions: Neutron and high-resolution synchrotron X-Ray diffraction study. *Applied physics letters*, 72(2):182–184, 1998.

[140] Q. Yu, C. Zhou, H. Zhang, and F. Zhao. Thermal stability of nanostructured 13 wt% Al2O3–8 wt% Y2O3–ZrO2 thermal barrier coatings. *Journal of the European Ceramic Society*, 30:889–897, 2010.

[141] D. Zhu, R. A. Miller, and D. S. Fox. Thermal and environmental barrier coating development for advanced propulsion engine systems. Technical report, Glenn Research Center, 2008.

[142] D. Zhu, R. A. Miller, and M. A. Kuczmarski. Development and life prediction of erosion resistant turbine low conductivity thermal barrier coatings. In *NASA/TM-2010-215669*, volume 215669, 2010.

[143] R. Zoughi. Microwave and millimeter wave nondestructive testing: A succinct introduction. *Research in Nondestructive Evaluation*, 7(2-3):71–74, 1995.